Internal alignments of red versus blue discs in dark matter haloes

Victor P. Debattista,[1]* Frank C. van den Bosch,[2] Rok Roškar,[3] Thomas Quinn,[4] Ben Moore[3] and David R. Cole[1]

[1]*Jeremiah Horrocks Institute, University of Central Lancashire, Preston PR1 2HE, UK*
[2]*Astronomy Department, Yale University, PO Box 208101, New Haven, CT 06520-8101, USA*
[3]*Research Informatics, Scientific IT Services, ETH Zürich, Weinbergstrasse 11, CH-8092, Zürich, Switzerland*
[4]*Astronomy Department, University of Washington, Box 351580, Seattle, WA 98195, USA*

ABSTRACT

Large surveys have shown that red galaxies are preferentially aligned with their haloes, while blue galaxies have a more isotropic distribution. Since haloes generally align with their filaments, this introduces a bias in the measurement of the cosmic shear from weak lensing. It is therefore vitally important to understand why this difference arises. We explore the stability of different disc orientations within triaxial haloes. We show that, in the absence of gas, the disc orientation is most stable when its spin is along the minor axis of the halo. Instead when gas cools on to a disc, it is able to form in almost arbitrary orientation, including off the main planes of the halo (but avoiding an orientation perpendicular to the halo's intermediate axis). Substructure helps gasless galaxies reach alignment with the halo faster, but has less effect on galaxies when gas is cooling on to the disc. Our results provide a novel and natural interpretation for why red, gas poor galaxies are preferentially aligned with their halo, while blue, star-forming, galaxies have nearly random orientations, without requiring a connection between galaxies' current star formation rate and their merger history.

Key words: Galaxy: halo – galaxies: evolution – galaxies: formation – galaxies: fundamental parameters – galaxies: haloes – galaxies: kinematics and dynamics.

1 INTRODUCTION

Intrinsic alignments of galaxies, i.e. correlations of galaxy shapes with each other or with the large scale density field, are one of the most important astrophysical contaminants for weak lensing measurements (see Troxel & Ishak 2015, for a comprehensive review). In particular, coherent alignments of the shapes of physically nearby galaxies can strongly bias the cosmic shear measurements that lie at the heart of upcoming experiments such as the Large Synoptic Survey Telescope (Ivezic et al. 2008), Euclid (Laureijs et al. 2011), the Dark Energy Survey (Soares-Santos & DES Collaboration 2012) and the *Wide-Field Infrared Survey Telescope* (Green et al. 2011). If ignored, this intrinsic alignment bias can cause large systematic errors in, for example, the inferred dark energy equation of state (e.g. Bridle & King 2007; Kirk et al. 2012). It is prudent, therefore, that we develop a solid understanding of galaxy alignments.

Observationally, various forms of alignment have been detected over a wide range of scales. On scales ranging from ∼1 to 100 h^{-1} Mpc, numerous studies have detected alignments between individual clusters (e.g. Binggeli 1982; Plionis 1994; Smargon et al. 2012), between galaxies (e.g. Pen, Lee & Seljak 2000; Brown et al.

2002; Heymans et al. 2004; Lee & Pen 2007; Okumura, Jing & Li 2009; Li et al. 2013), and between galaxies and their surrounding large-scale density (or tidal) field (e.g. Mandelbaum et al. 2006; Hirata et al. 2007; Paz, Stasyszyn & Padilla 2008; Faltenbacher et al. 2009; Tempel & Libeskind 2013; Tempel, Stoica & Saar 2013; Zhang et al. 2013, 2015). Alignments have also been detected on smaller scales, within individual host haloes. These include, among others, the alignment between brightest cluster galaxies and their parent cluster (e.g. Carter & Metcalfe 1980; Binggeli 1982; Struble 1990), between the orientation of central galaxies and the spatial distribution of their satellite galaxies (e.g. Sales & Lambas 2004; Brainerd 2005; Agustsson & Brainerd 2006; Yang et al. 2006; Azzaro et al. 2007; Faltenbacher et al. 2007; Wang et al. 2008a,b, 2010; Nierenberg et al. 2011; Li et al. 2013), as well as between the orientation of satellite galaxies and the central-satellite position vector (e.g. Pereira & Kuhn 2005; Agustsson & Brainerd 2006; Faltenbacher et al. 2007; Hao et al. 2011; Schneider et al. 2013). An important outcome from all these studies is that the strength of these various alignments depends on a variety of galaxy properties. Of particular relevance to this paper is the fact that the alignment effects are typically much stronger for red (early-type) galaxies than for blue (spiral) galaxies.

From the theoretical side, tidal torque theory predicts large-scale correlations between the angular momenta and shapes of dark matter

---

* E-mail: vpdebattista@gmail.com

haloes (e.g. Catelan & Porciani 2001; Catelan, Kamionkowski & Blandford 2001; Crittenden et al. 2001; Porciani, Dekel & Hoffman 2002), which has been tested and confirmed with numerical simulations (e.g. Croft & Metzler 2000; Heavens, Refregier & Heymans 2000; Jing 2002; Faltenbacher et al. 2008). The tidal field is however too weak to directly affect the orientation of galaxies and must do so either through formation or accretion processes (Camelio & Lombardi 2015). Simulations have also shown that the shapes and/or spins of dark matter haloes are aligned with their large-scale density distribution (e.g. Aragón-Calvo et al. 2007; Hahn et al. 2007a,b; Cuesta et al. 2008; Paz, Stasyszyn & Padilla 2008; Zhang et al. 2009; Wang et al. 2011; Codis et al. 2012; Libeskind et al. 2012; Trowland, Lewis & Bland-Hawthorn 2013). Such alignments originate from both tidal torques, and from the preferred accretion of new material along the directions of sheets and filaments that delineate the cosmic web (e.g. Jing 2002; Bailin & Steinmetz 2005; Faltenbacher et al. 2005). On small scales, inside the virialized regions of dark matter haloes, non-linear effects such as violent relaxation and impulsive encounters are believed to weaken any pre-infall alignments (e.g. Porciani et al. 2002). However, at the same time tidal forces due to the host halo may introduce new alignments, similar to the tidal-locking mechanism that affects the Earth–Moon system (e.g. Ciotti & Dutta 1994; Usami & Fujimoto 1997; Fleck & Kuhn 2003). Indeed, numerical simulations have shown that dark matter subhaloes are preferentially radially aligned, with their major axes pointing towards the centre of their host halo (e.g. Kuhlen, Diemand & Madau 2007; Faltenbacher et al. 2008; Pereira, Bryan & Gill 2008).

Hence, if *galaxy* shapes and/or orientations are determined either by the angular momentum or by the shape/orientation of the *halo* in which they form, then intrinsic galaxy alignments will naturally emerge. The vast majority of galaxies, including blue, spiral galaxies but also the majority of red, early-type systems, are supported by rotation (see e.g. Emsellem et al. 2011), and their orientation is therefore governed by angular momentum.[1] Thus, understanding intrinsic alignments requires understanding how the angular momentum vectors of discs align with their host haloes and their large-scale tidal field. Collisionless simulations find angular momenta of haloes aligned with their minor axes, with only small misalignments (Dubinski 1992; Warren et al. 1992; Porciani et al. 2002; Bailin & Steinmetz 2005; Faltenbacher et al. 2005). However, hydrodynamical simulations reveal a more complicated picture. First of all, even in the absence of cooling, the halo and gas angular momenta misalign on average by $\sim 30°$ (van den Bosch et al. 2002; Chen, Jing & Yoshikaw 2003; Sharma & Steinmetz 2005). Furthermore, when cooling is included, the formation of the disc modifies the shape and orientation of the inner halo, but leaves the outer halo largely intact (Kazantzidis et al. 2004; Bailin et al. 2005; Debattista et al. 2008, hereafter D08). Consequently, the disc angular momentum is well aligned with the inner halo ($r \lesssim 0.1 r_{\rm vir}$), but is only poorly aligned with the minor axis at larger halocentric radii; overall hydrodynamical simulations find that discs and haloes are misaligned by $30°$–$40°$ on average (Croft et al. 2009; Bett et al. 2010; Hahn, Teyssier & Carollo 2010). This is of the same order as what is required to reconcile the relatively weak alignment strength observed, with the relatively strong alignments predicted from pure dark matter simulations (e.g. Kang et al. 2007; Wang et al. 2008b; Joachimi et al. 2013b; Schneider et al. 2013; Zhang et al. 2015).

However, what is the cause of the colour-dependence of intrinsic alignment strength? It has been suggested (e.g. Joachimi et al. 2013a,b) that blue disc galaxies are aligned with the angular momentum vector of their host halo, while red, early-types have moments of inertia that are aligned with those of their host haloes. The latter is motivated by the belief that early-type galaxies are the outcome of major mergers, combined with the idea that merger remnants are oriented along the direction of the last major merger (e.g. van Haarlem & van de Weygaert 1993). However, as already alluded to above, the majority of red, early-type galaxies are discs: the ATLAS[3D] project finds that ~ 86 per cent of early-type galaxies (defined as galaxies that lack spiral arms) are rapidly rotating (Emsellem et al. 2011). Hence, we consider it unlikely that the origin of the different orientations of red versus blue galaxies is predominantly accounted for by mergers.

In this paper, we examine an alternative explanation that accounts for the fact that (i) dark matter haloes are triaxial (Bardeen et al. 1986; Barnes & Efstathiou 1987; Frenk et al. 1988; Dubinski & Carlberg 1991; Jing & Suto 2002; Bailin & Steinmetz 2005; Allgood et al. 2006), giving rise to torques between the halo and the disc, (ii) dark matter haloes have substructure, which can tilt discs (Huang & Carlberg 1997) and cause gravitational perturbations, and (iii) what distinguishes red from blue discs is the lack of ongoing gas accretion. In Debattista et al. (2013, hereafter D13), we explored the stability of disc galaxies with their spins along the intermediate axis of the halo, an orientation that has been proposed for the Milky Way (Law, Majewski & Johnston 2009; Law & Majewski 2010; Deg & Widrow 2013). D13 showed that such an orientation is never stable, and discs can never form in this orientation even when gas angular momentum is along the intermediate axis. D13 also showed that a disc can survive for a long time off one of the symmetry planes of the halo when gas is present, and proposed this as a natural interpretation for the Milky Way. In this paper, we extend this earlier work to address the stability of disc orientations in general, and the role of gas in supporting different orientations. We show that gas cooling provides a dominant mechanism for maintaining discs off the symmetry planes of the halo, and that this offers a natural explanation for the different orientations of red and blue galaxies. In particular, we suggest that red discs lack significant gas accretion, and have their orientation governed by halo torques, while blue discs have orientations that are set by the balance between halo torques and angular momentum of ongoing gas accretion.

2 COLLISIONLESS SIMULATIONS

We start by considering the evolution of disc galaxy orientation in the absence of complications introduced by gas.

2.1 Constructing collisionless initial conditions

As in D08, we form triaxial haloes via the head-on merger of two prolate haloes, themselves the product of head-on mergers of spherical haloes (Moore et al. 2004). The mergers, and all subsequent collisionless simulations, are evolved with PKDGRAV (Stadel 2001), an efficient, multi-stepping, parallel tree code.

In the collisionless simulations, we use halo A of D08. We have verified that other halo models give similar results. Halo A is constructed from two consecutive mergers. The first head-on merger places two concentration $\mathcal{C} = 10$ spherical haloes of mass $2.3 \times 10^{12}\,{\rm M_\odot}$ 800 kpc apart approaching each other at 50 km s^{-1}. The spherical haloes are generated from a distribution function

---

[1] Only the most massive ellipticals are pressure supported, and their orientations most likely reflect the directionality of their last major merger.

Table 1. The haloes used in the simulations of this paper. The properties listed are for the halo after the last merger and before the discs have been grown. N_p and N_g are the number of dark matter and gas particles within r_{200}, and M_{200} is the halo mass within the virial radius, r_{200}. Density axes-ratios b/a and c/a are by-eye averaged over the inner 20 kpc.

Halo	N_p (10^6)	N_g (10^6)	M_{200} ($10^{12}\,\mathrm{M_\odot}$)	r_{200} (kpc)	b/a	c/a
A	3.3	–	6.3	379	0.45	0.35
GP	1.4	1.3	1.6	239	0.55	0.55
GT	2.8	2.7	3.2	304	0.4	0.32

using the method of Kazantzidis, Magorrian & Moore ([2004](#)) with each halo composed of two mass species arranged on shells. The outer shell has more massive particles than the inner one, increasing the effective resolution in the centre. We use a softening parameter $\epsilon = 0.1\,\mathrm{kpc}$ ($\epsilon = 0.5\,\mathrm{kpc}$) for low (high) mass particles. As shown in D08, a large part of the particle mass segregation persists after the mergers and the inner region remains dominated by low-mass particles. This merger produces a prolate halo. Halo A results from the head-on merger of two copies of this prolate halo starting 400 kpc apart at rest. The progenitor spherical haloes each have 1 million particles, equally divided between their two mass species. The outer halo particles are $\sim$19 $\times$ more massive than the inner ones. Thus, in total halo A consists of 4 million particles. The shape of halo A was presented in D13; Table [1](#) lists its properties.[2] It has $c/a \sim 0.35$, but only a mild triaxiality (Franx, Illingworth & de Zeeuw [1991](#)) $T = (a^2 - b^2)/(a^2 - c^2) \simeq 0.9$ out to 100 kpc.

Once we produce the triaxial halo, we insert a disc of particles. The disc distribution is exponential with scalelength $R_d = 3\,\mathrm{kpc}$ in all cases except model LA2d, which had $R_d = 6\,\mathrm{kpc}$, and Gaussian scaleheight $z_d = 0.05R_d$. The discs are placed at various orientations within the halo. We refer to these experiments by the halo axis along which the disc's spin is aligned: in 'short-axis' (S) experiments, the disc spin is along the short axis of the halo, while in 'long-axis' (L) experiments, the disc spin is along the halo's long axis. An 'intermediate-axis' (I) experiment has the disc spin along the halo's intermediate axis. Most of the intermediate-axis simulations were presented already in D13; here, we include a new model, IA3, with a significantly more massive disc. The discs are comprised of 3×10^5 equal-mass particles. Initially the disc has negligible mass, but we increase this adiabatically linearly over time to a mass M_d. During this time, the halo particles are free to move and remain in equilibrium while the disc particles are held fixed in place.

Once the disc reaches the target mass, we set its particle kinematics appropriate for the constant disc-height z_d and Toomre-$Q = 1.5$, as described in Debattista & Sellwood ([2000](#)). For this, we calculate the potential using a hybrid polar-grid code with the disc on a cylindrical grid and the halo on a spherical grid (Sellwood [2003](#)). In setting up the disc kinematics, we azimuthally average radial and vertical forces. From these initial conditions, the models are then evolved with PKDGRAV, with timesteps refined such that $\delta t = \Delta t/2^n < \eta(\epsilon/a_g)^{1/2}$, where ϵ is the softening and a_g is the acceleration at a particle's current position. We use base timestep $\Delta t = 5\,\mathrm{Myr}$ in all cases except model SA1 (which uses $\Delta t = 50\,\mathrm{Myr}$). For all simulations, we use $\eta = 0.2$ and an open-

Table 2. The collisionless simulations of this paper. M_d is the mass of the disc, R_d is the disc exponential scale-length and z_d is the Gaussian scaleheight of the disc. All models are grown inside halo A.

Model	M_d ($10^{10}\,\mathrm{M_\odot}$)	R_d (kpc)	z_d (pc)
SA1	5.2	3	150
IA1	17.5	3	150
IA2	7.0	3	150
IA3	70.0	3	150
LA1	3.5	3	150
LA2	10.5	3	150
LA2d	10.5	6	300

ing angle of the tree code $\theta = 0.7$. Table [2](#) lists the collisionless simulations discussed in this paper.[3]

2.2 Briggs figures

The orientation of a disc inside a triaxial halo is necessarily a 3D property of a galaxy. Consequently visualizing this in a single 2D figure requires a projection and some loss of information. Because we are only interested in the orientation of the disc, which we quantify via the orientation of the disc angular momentum, it is sufficient to indicate the two orientation angles of the disc angular momentum. The lost information is the amplitude of the angular momentum vector, but this quantity is of no interest here. Briggs figures (Briggs [1990](#)), which are 2D polar coordinate representations of the direction of vectors, are ideal for this purpose. A Briggs figure plots the standard two spherical angular coordinates θ and ϕ as the radial and angle coordinates in 2D polar coordinates.

We use Briggs figures to present the evolution of the discs in our simulations relative to the dark matter halo. We hold the coordinate frame with respect to which the angles θ and ϕ are defined fixed, so changes in θ and ϕ are a result of disc tilting; because our haloes do not tumble (by construction) the directions of the principal axes of the halo, which we also indicate in the Briggs figures, do not change. Our long, short and intermediate axes are always defined at the virial radius, not at small radii where the halo shape is changed by the baryons. As our stellar discs are not strongly warped, we indicate only the orientation of the net angular momentum of the stars out to a radius of 15 kpc.

A note about how we indicate the principal axes in Briggs figures. We have chosen symbols in a simple visual mnemonic to indicate the short, intermediate and long axes: throughout we use a triangle, square and star, respectively, to represent them. Thus, the ordering of the axes is the same as the ordering of the number of sides in their corresponding symbols.

2.3 Evolution of the short-axis orientation

The top-left panel of Fig. [1](#) shows the evolution of model SA1 which starts with its disc spin along the short axis of the halo. The disc remains co-planar in this orientation for 10 Gyr, despite its low mass. The net potential is everywhere flattened in the same direction as the disc, even when only the halo potential is considered.

[2] We use a different convention for r_{200} from D08, Valluri et al. ([2010](#)) and Valluri et al. ([2012](#)), who used the radius *at* which $\rho = 200\rho_{crit}$. Here r_{200} is the radius *within* which the enclosed mass has average density $200\rho_{crit}$.

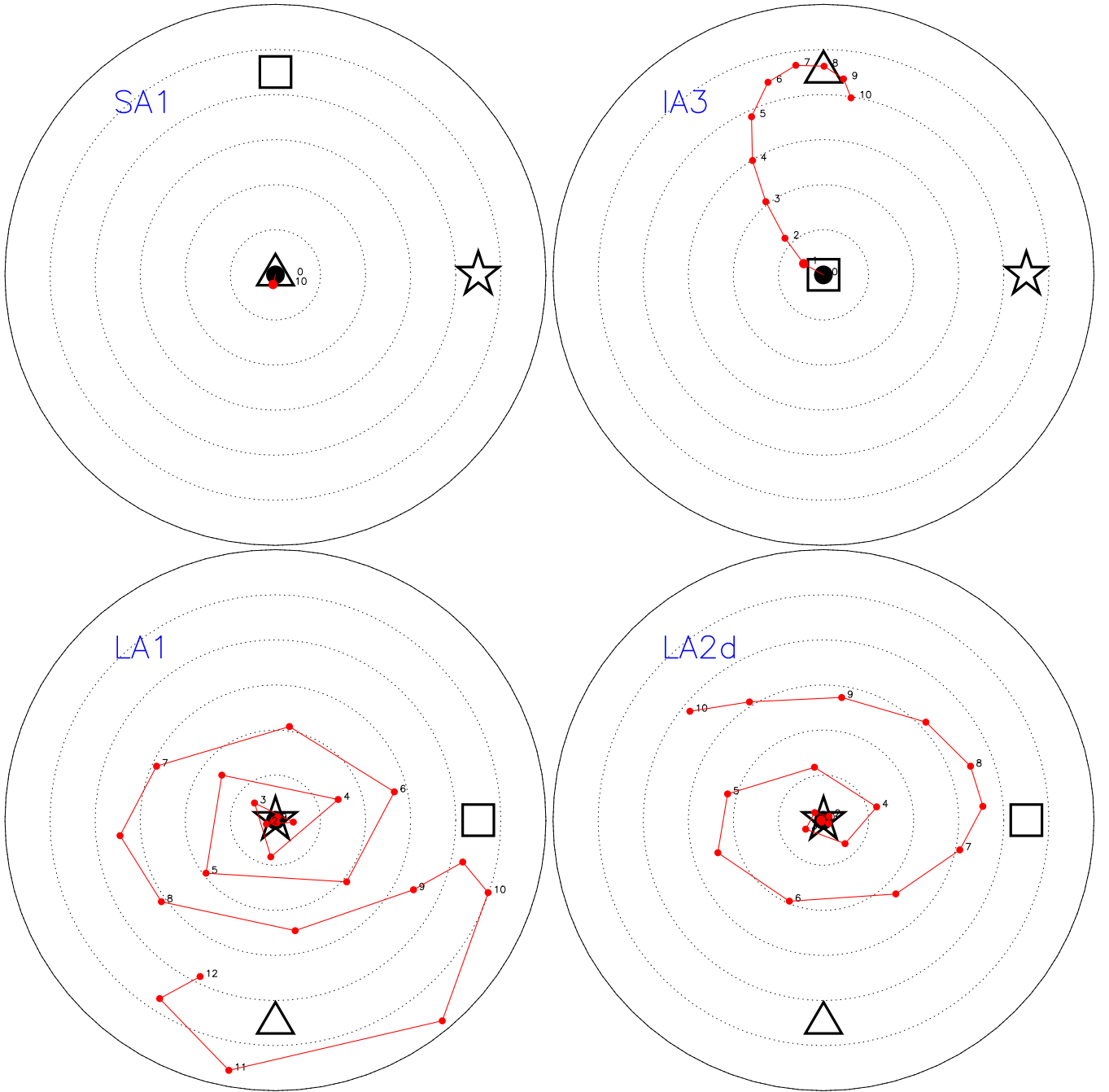[3] The names of models in this paper are different from those in D08.

Figure 1. Briggs figures (see Section 2.2 for an explanation of these figures) showing the evolution of models SA1 (top-left), IA3 (top-right), LA1 (bottom-left) and LA2d (bottom-right). Dotted circles are spaced at 20° intervals, with the outer solid circle corresponding to $\theta = 120°$ in each case. The disc spin is indicated by the big filled (black) circles at $t = 0$ and by the small filled (red) circles for later times. The small numbers besides some of the disc spins indicate the time. The open (black) star, square and triangle symbols indicate the direction of the long, intermediate and short axes of the haloes on large scales.

Small tilts of the disc therefore lead to torques which drive damped precession but do not lead to a runaway tilt, making this orientation stable.

2.4 Evolution of the intermediate-axis orientation

D13 showed that discs grown in halo A at the intermediate-axis orientation tilt very rapidly. They showed that this occurs even when the potential surrounding the disc is flattened by it to the

extent that its spin is along the potential's short axis. D13 argued that this indicates that the halo itself is unstable in this orientation. They presented evidence that orbits of dark matter particles that cross between the inner, flattened halo, and the outer elongated halo are unstable, which they proposed is the cause of the halo instability.

Here, we present another simulation, model IA3, of a disc in halo A with a mass $M_d = 7 \times 10^{11}$ M$_\odot$, i.e. four times more massive than the disc in model IA1, the most massive disc in halo A presented by D13. Fig. 2 shows the axes-ratios of the halo potential along the
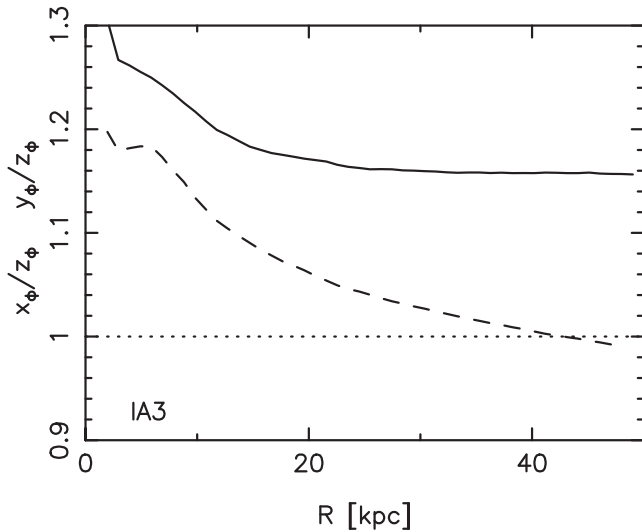
Figure 2. Halo only equipotential axes ratios in model IA3. The solid line shows x_Φ/z_Φ, while the dashed line shows y_Φ/z_Φ. The z-axis is perpendicular to the disc at $t = 0$.

principal axes x, y and z, with the z-axis perpendicular to the plane of the disc at $t = 0$. This figure shows that $x_\Phi/z_\Phi > 1$ and $y_\Phi/z_\Phi > 1$, i.e. the high-mass disc has flattened the halo so much that the short axis of the halo potential is vertical to the disc all the way out to 40 kpc. If the disc potential is included also, then the global potential becomes even more flattened along the disc's spin axis. Therefore, the disc, out to large radii, sits in a potential which never has its intermediate axis parallel to the disc spin axis. Naively then this orientation may be expected to be stable. Indeed when we evolve the system with the halo particles frozen in place, the disc remains in this orientation for 10 Gyr. However, this orientation is not stable when the halo particles are live, as can be seen in the top-right panel of Fig. 1. As did model IA1 of D13, the disc tilts away very rapidly from this orientation to a short-axis orientation.

2.5 Evolution of the long-axis orientation

The evolution of stellar discs placed with their spin along the long axis of the halo depends on the shape of the halo potential within which the disc is immersed. In model LA1, the low-mass disc is quickly driven off its original plane and precesses rapidly around the long axis while slowly tilting towards an orthogonal orientation. This precession ends abruptly when the disc reaches a nearly intermediate-axis orientation; after this the disc drops towards a short-axis orientation, precessing slowly about this orientation, as shown in bottom-left panel of Fig. 1. The more massive disc in model LA2 does not tilt much, only reaching $\theta \simeq 15°$ after 10 Gyr, but it precesses about the long axis.

An explanation for why LA1 tilts while LA2 appears stable can be obtained from Fig. 3, which shows the profile of the axis-ratios of the potential along the three principal axes, x, y and z with the z-axis perpendicular to the disc. Close to the centre of the galaxy, the equipotentials are flattened like the disc ($x_\Phi/z_\Phi \simeq y_\Phi/z_\Phi > 1$), becoming almost prolate and orthogonal to the disc further out ($x_\Phi/z_\Phi \simeq y_\Phi/z_\Phi < 1$). The entire disc in model LA1 sees an orthogonal prolate halo potential; the top panel of Fig. 3 shows that, for the halo potential, $\Phi_x/\Phi_z \simeq \Phi_x/\Phi_z < 1$. Thus, this orientation is unstable and any small perturbation of the orientation leads to the disc being torqued out of its original plane. In model LA2, instead a
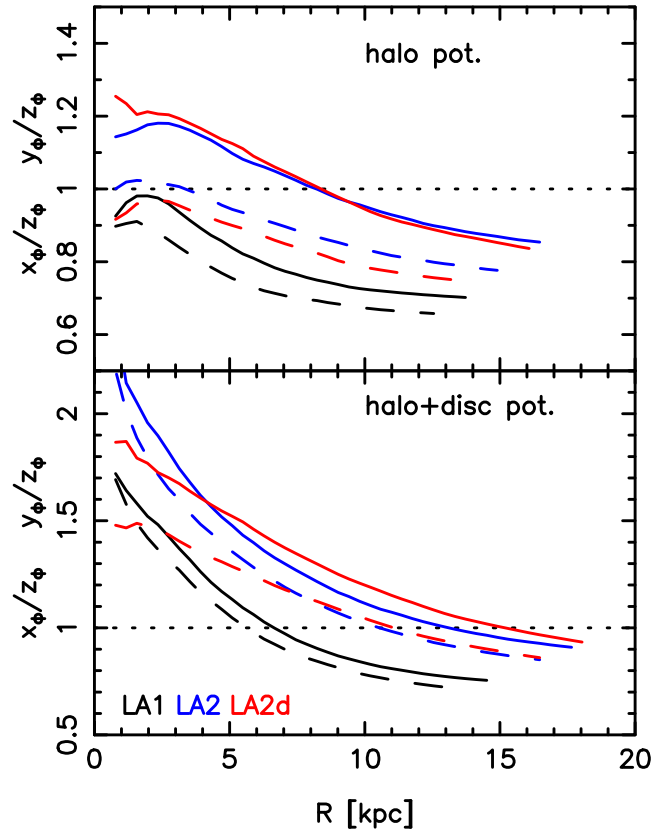

Figure 3. Equipotential axes ratios in models LA1 (black lines), LA2 (blue lines) and LA2d (red lines). The solid lines show x_Φ/z_Φ, while the dashed lines show y_Φ/z_Φ, where $z > x > y$ are the halo's long, intermediate and short axes on large scales and the z-axis is perpendicular to the disc. The dotted horizontal lines indicate an axis ratio of unity; if both axes-ratios follow this line then the potential is spherical. The top panel shows the shape of the halo potential only, while the bottom one shows the shape of the full potential.

large part of the disc is surrounded by a halo potential which is vertically flattened ($\Phi_x/\Phi_z > 1$). Thus, small perturbations do not lead to strong torques in model LA2, so it lasts in this orientation longer. We test this interpretation in model LA2d, in which a disc with the same mass as in LA2 but with a larger scalelength, $R_d = 6$ kpc, is grown in halo A. The shape of the resulting potential is presented in Fig. 3; this is not much different from LA2. However, now a smaller mass fraction of the disc is covered by a vertically flattened halo potential. As a result, while model LA2 only tilted by $\sim 10°$, model LA2d tilts by $\sim 80°$, as shown by the Briggs figure at bottom-right of Fig. 1. Fig. 4 compares the evolution of the tilt in LA2 and LA2d; while the tilt angle of model LA2 grows slowly, model LA2d, which has about twice the angular momentum, nonetheless tilts rapidly. This shows that it is the disc material sitting outside the vertically flattened potential that is responsible for the fast tilting in the long-axis orientation.

2.6 Synthesis of collisionless simulations

Fig. 5 compares the tilting of all the long- and intermediate-axis simulations in halo A. The intermediate-axis simulations most rapidly reach the short-axis orientation. At low disc mass, the long-axis orientation is unstable with the disc tilting and precessing. At high disc mass, the long-axis orientation is still unstable, but now the
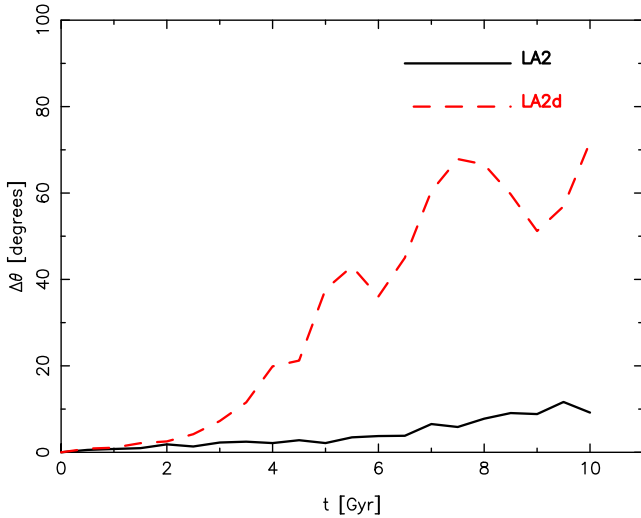
Figure 4. Evolution of the angle between the instantaneous stellar angular momentum and the initial one in models LA2 and LA2d. Both models start in a long-axis orientation in the same halo and have the same mass. Model LA2d has a scalelength twice that of LA2.
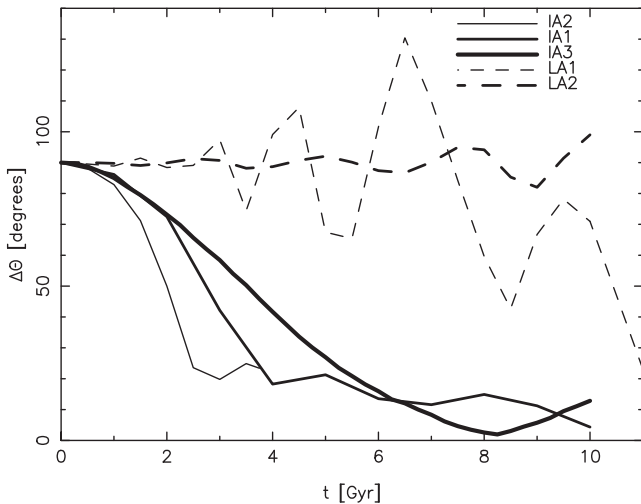

Figure 5. Evolution of the angle between the stellar disc angular momentum and the halo short axis at large radius. Solid lines are models with discs starting in the intermediate-axis orientation and dashed lines are for those starting in the long-axis orientation, as indicated at top-right. All models are evolved in halo A.

tilting rate is so low that the disc persists close to this orientation for most of a Hubble time. However, the fact that this orientation is only quasi-stable suggests that it may be susceptible to perturbations from satellites, as we demonstrate below.

Comparing the discs during the period when the disc mass is growing (with the disc particles fixed in place and the halo particles free to move), we find that the disc in the short-axis orientation has a potential energy ~1 per cent smaller (more bound) than the disc in the long-axis orientation for the same mass, making it the most stable orientation. In a fixed halo potential, it is readily apparent that the disc potential is minimized when the disc is in a short-axis orientation; this is still true even when the inner halo is flattened by the disc growing within it.

3 THE IMPACT OF COOLING GAS

Although dark matter angular momentum tends to align with the halo's short axis, cosmological simulations show that the gas angular momentum is frequently decoupled from that of the halo (van den Bosch et al. 2002; Chen et al. 2003; Bailin et al. 2005; Sharma & Steinmetz 2005; Roškar et al. 2010). We now explore how the delivery of gas with angular momentum along different directions affects the evolution of disc orientation.

3.1 Initial conditions with gas

We perform experiments of discs forming out of gas cooling within both prolate and fully triaxial haloes. All stars in these simulations form self-consistently out of the cooling gas. As did Aumer & White (2013), in early experiments we found that arbitrarily inserting rotating gas coronae within pre-existing triaxial dark matter haloes leads to a substantial loss of gas angular momentum, making the formation of realistic disc galaxies difficult. Our approach therefore is to include the gas right from the start while constructing the prolate/triaxial dark matter haloes via mergers. We set up a prolate halo with an equilibrium gas distribution by the head-on merger of two spherical Navarro-Frenk-White dark matter haloes each with an embedded spherical hot gas component containing 10 per cent of the total mass and following the same density distribution. The starting haloes are set up as described in Roškar et al. (2008): each has a mass within the virial radius ($r_{200} \simeq 200$ kpc) of 10^{12} M$_\odot$. A temperature gradient in each corona ensures an initial gas pressure equilibrium for an adiabatic equation of state. Gas velocities are initialized to give a spin parameter of $\lambda = 0.065$ (Bullock et al. 2001; Macciò et al. 2007), with specific angular momentum $j \propto R$, where R is the cylindrical radius. Each halo uses 1×10^6 particles in each of the gas and dark components. Gas particles initially have masses 1.4×10^5 M$_\odot$ and softening 50 pc, the latter inherited by the star particles, while dark matter particles come in two mass flavours (10^6 M$_\odot$ and 3.5×10^6 M$_\odot$ inside and outside 200 kpc, respectively) and with a softening of 100 pc. Initially the two haloes are 500 kpc apart and moving towards each other at a relative velocity of 100 km s^{-1}, producing prolate systems. We generate three such prolate haloes differing by the orientation of the gas angular momentum relative to the halo long axis. Since the remnant's long axis is along the initial separation vector, we only need to incline the initial spherical gas haloes relative to the separation vector to ensure a remnant with gas angular momentum tilted relative to the halo long axis. We chose tilt angles of 0°, 45° and 90° (models GPL, GP45, and GPS, respectively). Fig. 6 shows the merger geometries of the three prolate haloes. The final haloes are quite prolate, $T \gtrsim 0.95$, and have $<c/a> \simeq 0.65$ (see Fig. 7).

We produce triaxial models by merging two copies of the prolate system GPS. By judicious orientation of the angular momenta before the merger, we are able to produce systems with angular momentum along either the long or the intermediate axes, which we refer to as models GTL and GTI, respectively. Model GTI was presented in D13. In models GTI and GTL, we first rotate GPS about the long axis so the angular momentum vector is along the y-axis, then rotate the system about the z-axis by $\pm 30°$. Merging these from a separation of 500 kpc with a relative velocity of 100 km s^{-1} produces a triaxial system with long, intermediate and short axes corresponding to the x, y and z axes, respectively. The merger geometries for these models are shown in Fig. 8. We also ran an additional model with gas angular momentum initially in the plane spanned by the long and intermediate axes (model GTE). We
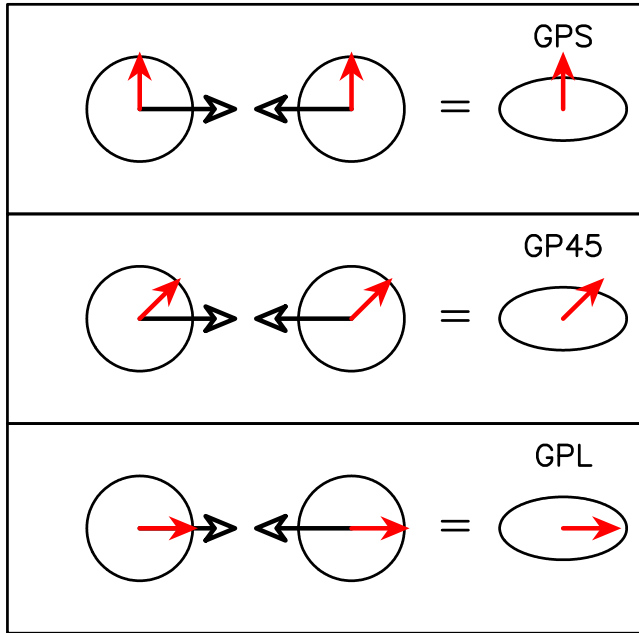
Figure 6. Cartoons showing the merger geometries that produce the prolate models GPS, GP45 and GPL. The (red) filled arrows indicate the orientation of the gas angular momentum, while the (black) open arrows show the merging velocities of the spherical haloes. The final long axis of the merger remnant is along the merging direction.
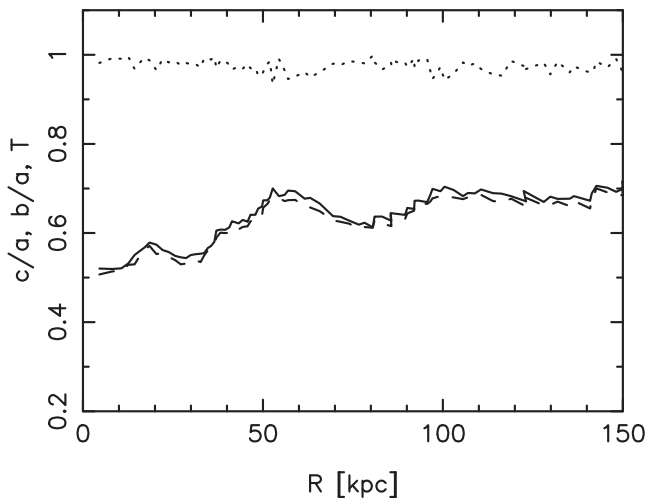

Figure 8. Cartoons showing the merger geometries that produce the triaxial models GTL, GTI and GTE. The (red) filled arrows indicate the orientation of the gas angular momentum relative to the haloes, while the (black) open arrows show the merging velocities of the spherical haloes. The coordinate axes are indicated in the top panel: the long axis of the merger remnant is along the x-axis while the short axis is perpendicular to the sheet (z-axis). The intermediate axis is along the y-axis.

Figure 7. The shape of the dark matter density for the haloes of models GPL, GPS and GP45. Solid, dashed and dotted lines show b/a, c/a and T, respectively. The three haloes have identical shape.

produce this model by rotating GPS about the y-axis by 90° as before, then merging two copies of this system *both* rotated about the z-axis by −30°. This merger geometry is also shown in Fig. 8. By construction, none of the prolate and triaxial haloes have any figure rotation. The shape of the three triaxial haloes is identical and is shown in fig. 1 of D13.

These simulations are evolved with GASOLINE (Wadsley, Stadel & Quinn 2004), the smoothed particle hydrodynamics (SPH) version of PKDGRAV. We use a timestep of 10 Myr with a refinement parameter $\eta = 0.175$. During the merger, and for some time thereafter, we
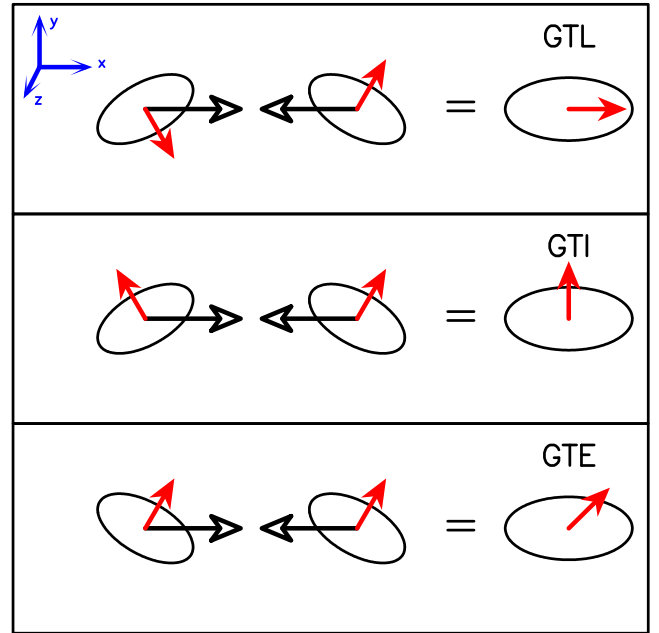
evolve the system adiabatically without any star formation. Then we switch on gas cooling, star formation and stellar feedback using the prescriptions of Stinson et al. (2006). A gas particle undergoes star formation if it has number density $n > 0.1\,\mathrm{cm}^{-3}$, temperature $T < 15\,000$ K and is part of a converging flow; efficiency of star formation is 0.05, i.e. 5 per cent of gas eligible to form stars does so per dynamical time. Star particles form with an initial mass of 1/3 that of the gas particle, which at our resolution corresponds to $4.6 \times 10^4\,\mathrm{M}_\odot$. Gas particles can spawn multiple star particles but once they drop below 1/5 of their initial mass the remaining mass is distributed amongst the nearest neighbours, leading to a decreasing number of gas particles. Each star particle represents an entire stellar population with a Miller–Scalo (Miller & Scalo 1979) initial mass function. The evolution of star particles includes feedback from Type II and Type Ia supernovae, with their energy injected into the interstellar medium (ISM). The effect of the supernovae explosions is modelled at the sub-grid level as a blastwave propagating through the ISM (Stinson et al. 2006). We also include feedback from asymptotic giant branch stellar winds. We use an opening angle of $\theta = 0.7$. The timestep of gas particles also satisfies the condition $\delta t_{\mathrm{gas}} = \eta_{\mathrm{courant}} h/[(1 + \alpha)c + \beta\mu_{\mathrm{max}}]$, where $\eta_{\mathrm{courant}} = 0.4$, h is the SPH smoothing length, α is the shear coefficient, which is set to 1, $\beta = 2$ is the viscosity coefficient and μ_{max} is described in Wadsley et al. (2004). The SPH kernel is defined using the 32 nearest neighbours. Gas cooling is calculated without taking into account the gas metallicity. These prescriptions have been shown to lead to realistic Milky Way-type galaxies (Roškar et al. 2012; Roškar, Debattista & Loebman 2013). We set $t = 0$ to be the time at which we switch on gas cooling and star formation.

Table 3. The simulations with gas and star formation. N_* and M_* are the number and the mass of star particles at the final step. λ is the angular momentum parameter (computed using equation 1) at $t = 0$, when we turn on gas cooling and star formation.

Model	Halo	N_* (10^6)	M_* $(10^{10} \, M_\odot)$	λ
GPS	GP	3.16	9.4	0.058
GP45	GP	3.16	9.5	0.055
GPL	GP	3.29	9.9	0.047
GTI	GT	6.97	20.7	0.021
GTL	GT	7.10	21.1	0.020
GTE	GT	6.69	19.9	0.029

Table 3 lists all the gas+star formation simulations. It includes the value of λ (Bullock et al. 2001), the angular momentum parameter of the gas. This is defined as

$$\lambda = \frac{L_g}{GM_t} \sqrt{\frac{|E_g|}{M_g^3}}, \qquad (1)$$

where L_g, E_g and M_g is the angular momentum, energy and mass of the gas within the virial radius, and M_t is the total (gas+dark matter) mass within the same radius. As Fig. 6 suggests, the merger geometry should result in all the prolate halo models having the same gas angular momentum. Instead λ increases as the angular momentum direction changes from the long to the short axis, indicating that angular momentum is being transported within the gas corona.

3.2 Evolution of disc orientation in prolate haloes with gas

We start by considering the simpler evolution of discs forming in prolate haloes in which the initial gas angular momentum is inclined to the halo long axis by $0°$ (model GPL), $45°$ (model GP45) and $90°$ (model GPS).

After 8 Gyr, all three systems form stellar discs of comparable mass. Model GPS forms a stellar disc with its spin perpendicular to the halo's long axis and remains in this orientation throughout its evolution. Within 1 Gyr the disc spin in model GPL settles almost into alignment with the long axis to within $5°$, where it remains. Even when we shut off gas cooling at 4 Gyr, the disc still remains in a long-axis orientation, in good agreement with the results of the collisionless simulations.

The most interesting result of these simulations comes from model GP45. In this model, the stellar disc never settles to one of the main planes of the halo. Nor does the disc line up with its angular momentum parallel to that of the gas. Instead, as Fig. 9 shows, the two angular momenta are misaligned by $\sim 65°$ and remain in this orientation without precessing throughout the simulation. Fig. 10 shows the dark+stellar mass distribution at 8 Gyr, clearly showing a stellar disc tilted relative to the main planes of the halo. The halo is misaligned with the disc already at 20 kpc, which is well within the region where the halo of the Milky Way is probed by the Sagittarius tidal stream. Modelling the Sagittarius stream therefore requires that the tilt of the dark matter halo relative to the disc also be taken into account. Interior to this region, the halo is flattened by the growing stellar disc.

How is the disc able to remain in this orientation? We compute the torque on the stellar disc by first computing the forces on the stars using GASOLINE in the usual way. The net torque on the disc is
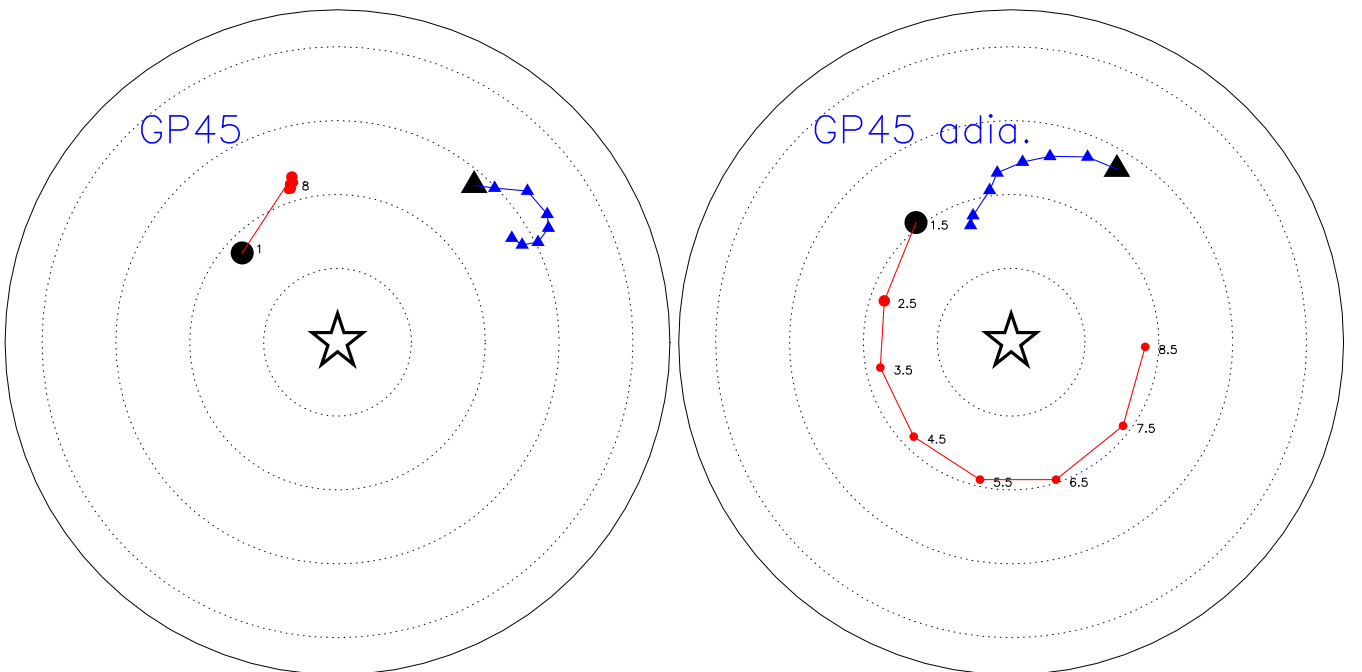

Figure 9. Left: Briggs figure for model GP45 showing 8 Gyr of evolution. Right: Briggs figure for model GP45 when gas cooling is turned off after 1 Gyr. Dotted circles are spaced by $20°$. The disc spin is indicated by the filled (red and black) circles. The (blue and black) filled triangles mark the orientation of the hot gas angular momentum between 20 kpc and 50 kpc. The spin of both the disc and gas at 1 Gyr (left) and 1.5 Gyr (right) are marked by the larger (black) corresponding symbols. The long axis corresponds to the open (black) star. The outer solid circle corresponds to $\theta = 90°$; since this is a prolate (axisymmetric) halo each point on this circle corresponds to a short axis of the halo.

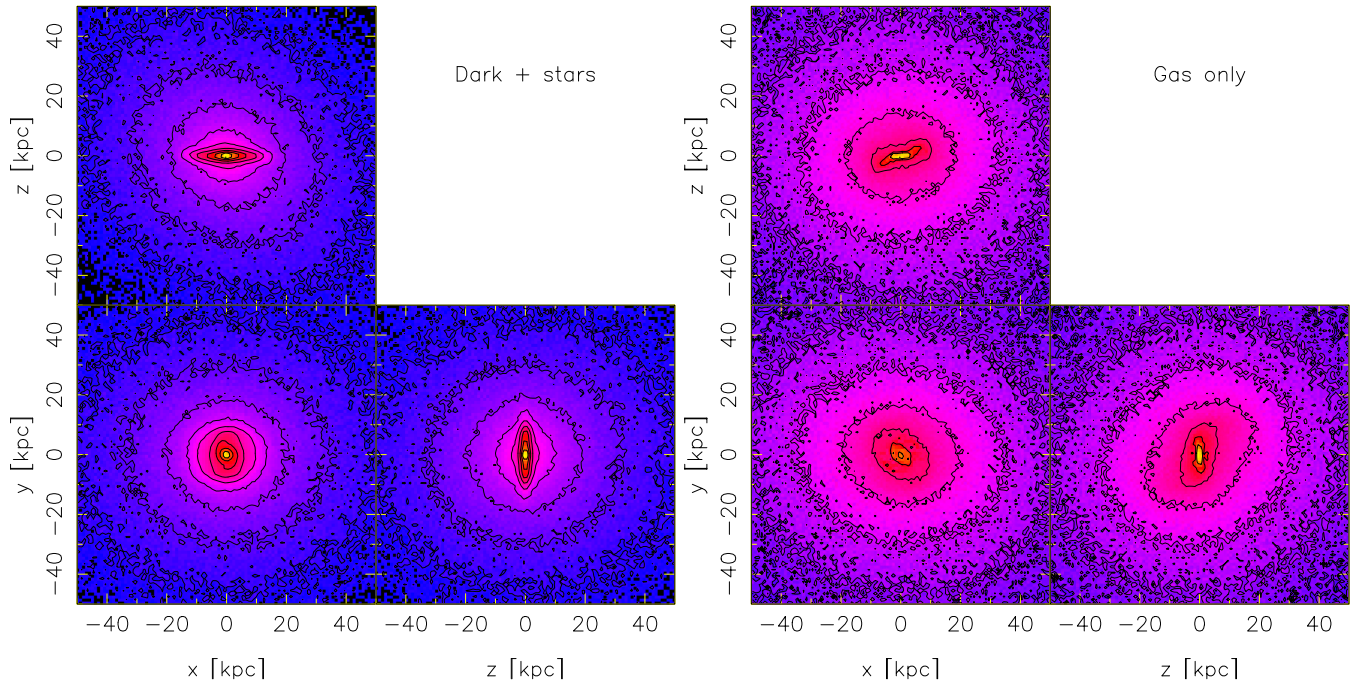**Figure 10.** Model GP45 at 8 Gyr with the system rotated so the disc is in the (x, y)-plane and the halo long-axis is in the (x, z)-plane. Left: Disc+halo mass distribution. The contribution of the stars has been increased by a factor of $10 \times$ to make the disc more apparent. Right: gas mass distribution at the same orientation.

then given by

$$\tilde{\tau} = \sum_i m_i \boldsymbol{r}_i \times \boldsymbol{F}_i, \tag{2}$$

where the sum is over all star particles and m_i, $\boldsymbol{r}_i$ and $\boldsymbol{F}_i$ are the mass, position vector (relative to the centre of the galaxy) and force on the ith star particle. We compute the torques on the stars from the dark matter halo (τ_h) and from the gas (τ_g) separately. Fig. 11 presents the torques on the stellar disc at $t = 8$ Gyr. We also show the angular momentum of gas within 25 kpc at $T < 10^6$ K (J_g); this gas, which is destined to cool on to the stellar disc, arrives tilted with respect to its plane. As the gas cools from large distances, it feels the gravitational torque from the halo and its gains angular momentum along this direction. Once the gas reaches the region dominated by the stellar disc, its spin axis gains a component orthogonal to the τ_g direction, due to the torque it feels from the disc, before settling into the disc. The right-hand panel of Fig. 10 shows that the cooling gas reaches the centre in a warped disc. The stellar disc, therefore, is absorbing from the cooling gas angular momentum in the direction opposite to the direction in which the halo torque is pulling it. As a result, equilibrium between the gravitational torques and the gas inflow has been established. The equilibrium is not driven by the regulation of the gas inflow rate since the mass of the final disc is very similar in this model and models GPL and GPS. Rather, the equilibrium is determined by the disc settling into an orientation where the tilting that would be induced by all torques on it and the tilting that the accreting gas angular momentum would cause cancel each other out. If the angular momentum orientation of the cooling gas changes with time, then the equilibrium orientation of the disc must also evolve. We show an example of such evolution below.

Fig. 12 shows the evolution of the mass and angular momentum of the stellar and cool gas discs (defined as all gas within 50 kpc at

temperature $T < 10^5$ K). By 5 Gyr the cold gas fraction of the galaxy has fallen to $\lesssim 5$ per cent of the stellar mass. The stellar disc mass and angular momentum is growing at a much higher rate than the gas disc is declining, which is possible because gas is continuously cooling on to the disc. Over the duration of the simulation, the cool gas net mass and angular momentum change is a small fraction of that of the stars, indicating that the gas mass reaches a detailed balance between inflow and loss from star formation and feedback. The bottom panel of Fig. 12 compares the gravitational torques on the stars and the rate of change of stellar angular momentum:

$$\left. \frac{|\Delta \boldsymbol{L}|}{\Delta t} \right|_{t_2} = \frac{|\boldsymbol{L}_2 - \boldsymbol{L}_1|}{t_2 - t_1}. \tag{3}$$

The rate of change of stellar angular momentum generally exceeds the direct gravitational torque from the dark halo and gas corona in spite of the strongly prolate ($b/a \lesssim 0.7$ within 50 kpc) halo. The continuous delivery of angular momentum misaligned with the stellar disc's therefore explains why the stellar disc is able to persist misaligned relative to the halo.

When the gas can cool, the disc reaches a dynamical equilibrium and does not change its orientation significantly; without cooling gas the disc must precess about the long axis. An example of this precession, with cooling turned off and evolved adiabatically after 1 Gyr (when the stellar mass is 15 per cent of its final mass) is shown in the right-hand panel of Fig. 9. The precession is not accompanied by a significant tilting away from the long axis in this prolate halo. We also verified that the disc precesses without tilting significantly when gas cooling is shut off at a later time when the stellar disc is more massive.
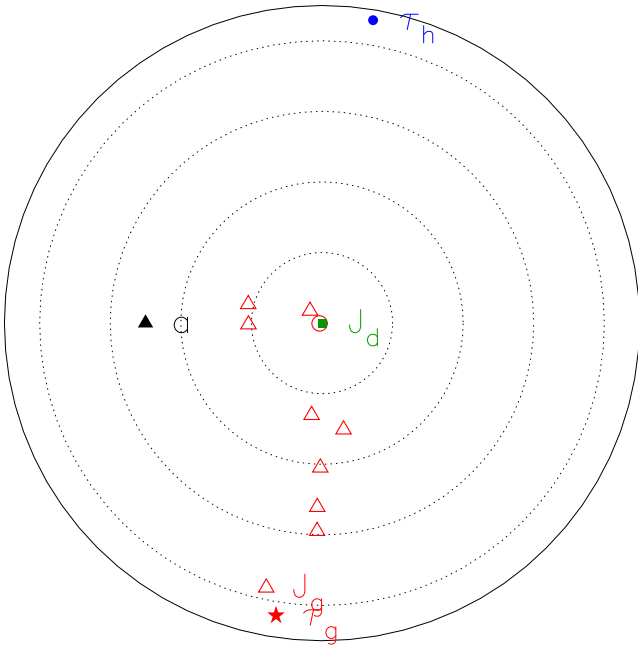
Figure 11. Briggs figure showing the gravitational torques and angular momenta in model GP45 at 8 Gyr. The dotted circles are spaced by 20° intervals with the outer solid circle at 90°. The system has been re-oriented, as in Fig. 10, such that the disc's angular momentum, indicated by the solid (green) square, is along the z-axis (the origin), while the halo long axis (indicated by the filled, black triangle) is in the (x, z)-plane. The solid (blue) circle indicates the torque, τ_h, on the stars from just the dark matter halo (outside 25 kpc), while the filled (red) star indicates the torque, τ_g, on the stars from the gas. The open (red) circle and triangles represent the *angular momentum* of cool ($T < 10^5$ K) gas within the inner 25 kpc in 10 annuli, with the central annulus indicated by the open circle.

3.3 Evolution of disc orientation in triaxial haloes with gas

Having understood the role of gas cooling in establishing a dynamical equilibrium which maintains stellar discs off the principal planes in prolate haloes, we now consider the more complicated fully triaxial models.

3.3.1 The long-axis orientation

The top-left panel of Fig. 13 shows the evolution of model GTL. The disc forms nearly perpendicular to the halo long axis and remains in this orientation for the 9 Gyr of its evolution, in agreement with the evolution of model GPL in the prolate halo.

3.3.2 The intermediate-axis orientation

D13 presented the evolution of model GTI.[4] Briefly, D13 showed that the disc that forms in this model never settles into an intermediate-axis orientation, even though the gas angular momentum is along the intermediate axis. This tilting can be seen in the bottom-left panel of Fig. 13. The failure to settle into an intermediate-axis orientation occurs despite the fact that the inner halo surrounding the disc is flattened vertically like the disc, so that the disc sees only a potential with a short axis perpendicular to it. D13 argued that the intermediate axis orientation, which has been

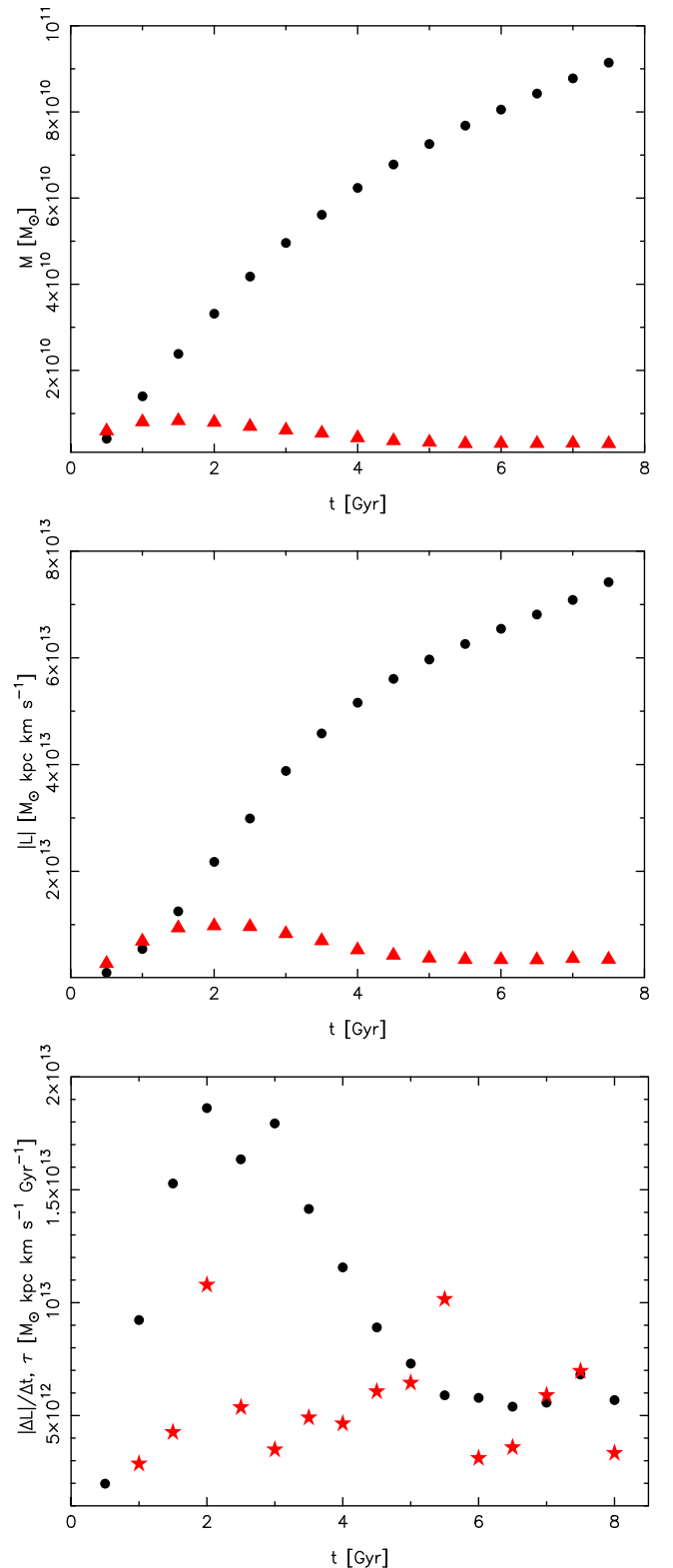[4] D13 refer to this model as GI1.

Figure 12. The evolution of the mass (top panel) and angular momentum (middle panel) in model GP45. The (black) circles show the stellar disc while the (red) triangles show the cool ($T < 10^5$ K) gas disc. The bottom panel shows the rate of change of total angular momentum of the stars, indicated by the (black) circles, and the (full) gravitational torques on the stars, indicated by the (red) filled stars.
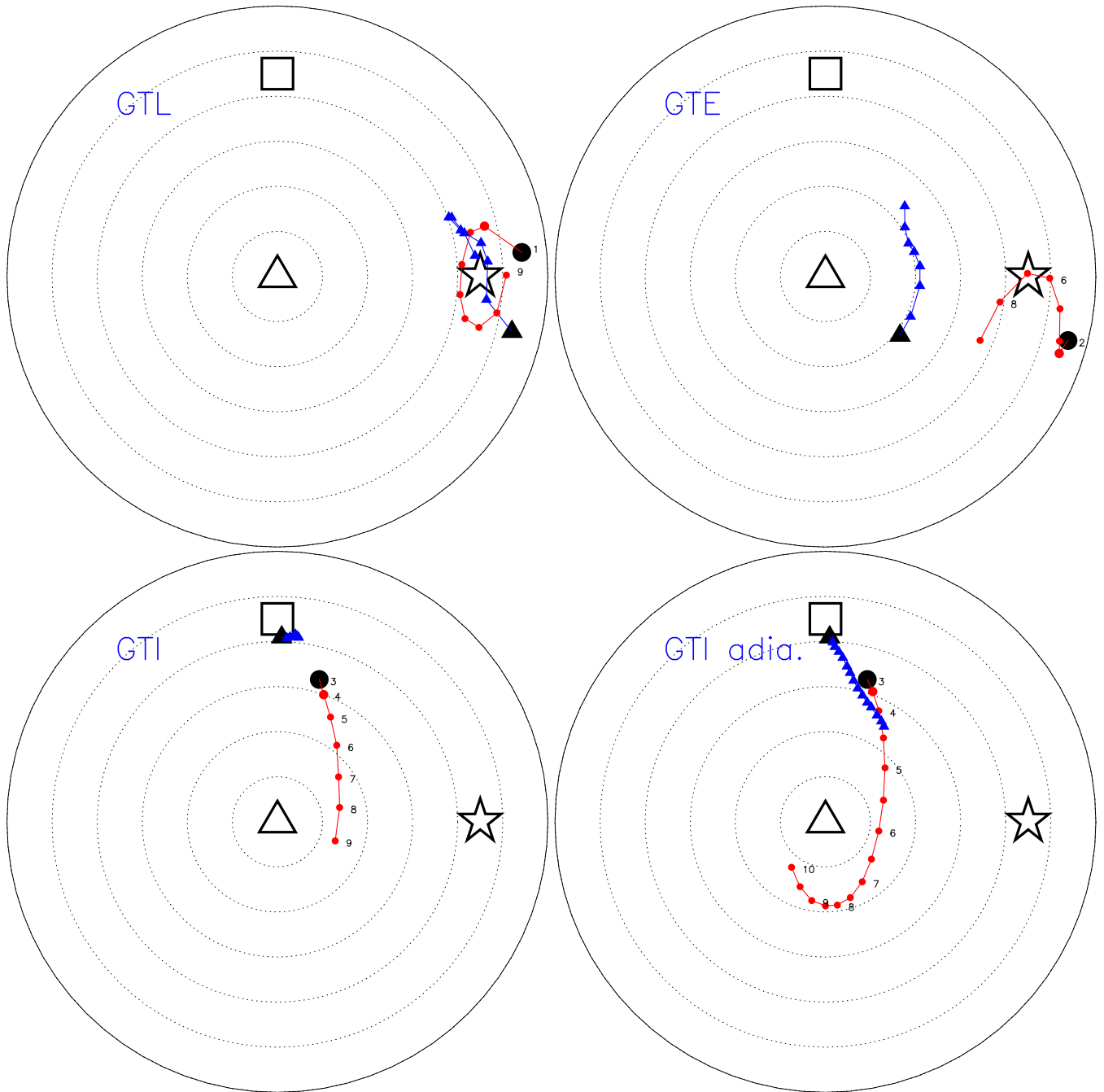
Figure 13. Briggs figures showing the evolution of models GTL (top-left), GTE (top-right), GTI (bottom-left) and GTI with star formation switched off after 3 Gyr (bottom-right). Dotted circles are spaced by 20°. The disc spin is indicated by the filled (red and black) circles. The (blue and black) filled triangles mark the orientation of the hot gas angular momentum between 20 kpc and 50 kpc. The spin of both the disc and gas at 1 Gyr (first output in GTL, top-left panel), 3 Gyr (when the disc settles in model GTI, bottom-left panel and star formation turned off, bottom-right panel) and 2 Gyr (coherent disc formed in GTE, top-right panel) are marked by the larger (black) corresponding symbols. The long, intermediate and short axes of the haloes correspond to the (black) open star, square and triangle symbols. The outer solid circle corresponds to $\theta = 120°$.

suggested for the Milky Way (Law et al. 2009; Law & Majewski 2010; Deg & Widrow 2013; Vera-Ciro & Helmi 2013), is unstable *for the halo* and therefore very implausible.

The bottom-right panel of Fig. 13 shows the effect of inhibiting gas cooling after 3 Gyr (by which point the disc has already attained ∼50 per cent of its final mass). Then the disc tilts rapidly towards a short-axis orientation. Compared with the gas cooling case (fig. 11 of D13), the stellar disc approaches the short-axis orientation much

more rapidly when gas does not cool, with a tilting rate almost twice that of GTI and comparable to the one in models IA1 and IA2 without gas.

3.3.3 Model with evolving gas angular momentum orientation

The top-right panel of Fig. 13 shows the evolution of model GTE. In this model, the mergers are set up such that the gas net angular

momentum is initially in the plane spanned by the long and inter-mediate axes. However, torques on the corona from the halo and angular momentum transport result in an inner ($20 \leq r \leq 50$ kpc) gas corona with angular momentum precessing slowly about the halo's short axis. Between 4 and 7 Gyr this angular momentum is within $\sim20°$ of the plane spanned by the short and long axes of the halo, enabling the stellar disc to grow in an almost long-axis orientation. Indeed at 7 Gyr the disc is perpendicular to the halo's long axis. Yet once the gas angular momentum evolves away from this plane, it drags the stellar disc off the long-axis orientation by more than $20°$. That gas can drive a disc off an equilibrium orientation demonstrates that gas cooling plays a dominant role in determining the relative orientations of discs and haloes.

4 THE EFFECT OF SATELLITE PERTURBATIONS

We now explore the effect of substructure on disc orientations in the absence of gas by introducing a satellite in models SA1 and LA2. We use a concentration $c = 12$ halo of mass $1.3 \times 10^{11}\,M_\odot$ (i.e. ~2 per cent of M_{200} for halo A). We place it at 150 kpc on the halo's long axis and give it a tangential velocity such that its orbital pericentre is at ~10 kpc. In both cases, the satellite disrupts by 2 Gyr. The top panel of Fig. 14 shows the effect of this perturbation: while SA1 quickly returns to a nearly short-axis orientation, the more massive LA2 slowly tilts away from its original orientation for the remainder of its evolution. These small perturbations show that the long-axis orientation is only quasi-stable even when the disc is massive. The bottom panel of Fig. 14 shows a Briggs figure of the evolution of the orientation of model LA2 perturbed by the satellite. After the initial perturbation the disc precesses about the long axis, slowly moving away from that orientation. This precession indicates that the tilting is driven by the direct torquing from the halo, rather than a lingering influence of the satellite. The effect of the satellite therefore is only to provide the initial perturbation that drives the disc from the local energy minimum in the long-axis orientation.

To test the effect of substructure when gas is present, we insert the same satellite into the prolate model GPL at 4 Gyr, at which point the stellar disc has a mass of $6.6 \times 10^{10}\,M_\odot$. The satellite mass represents 8 per cent of M_{200} for halo GP. The satellite is placed at 150 kpc on the halo's long axis and has a tangential velocity such that its pericentre is at 20 kpc; the satellite disrupts by 2 Gyr. Fig. 15 shows the evolution of the system when gas is allowed to cool and when gas is adiabatic. Both discs tilt away from their initial orientation; the case with no gas cooling tilts faster and further than the case with gas cooling. In the latter case, the disc tilting follows the angular momentum of the gas corona, while when gas is not cooling the stellar disc tilts independently of it.

Finite perturbations from substructures will therefore destabilize galaxies in the long-axis orientation. When gas cools on to the disc, it slows down the tilting but the disc never returns to a long-axis orientation. Infalling satellites also impart angular momentum to the gas corona, further driving the disc off the long-axis orientation.

5 DISCUSSION

5.1 Cosmological effects not considered

Valluri et al. (2013) showed that the orbital structure of a dark matter halo surrounding a Milky Way-sized galaxy that forms in a fully cosmological model is not much different from isolated triaxial haloes, including some of the ones considered here. Thus, from
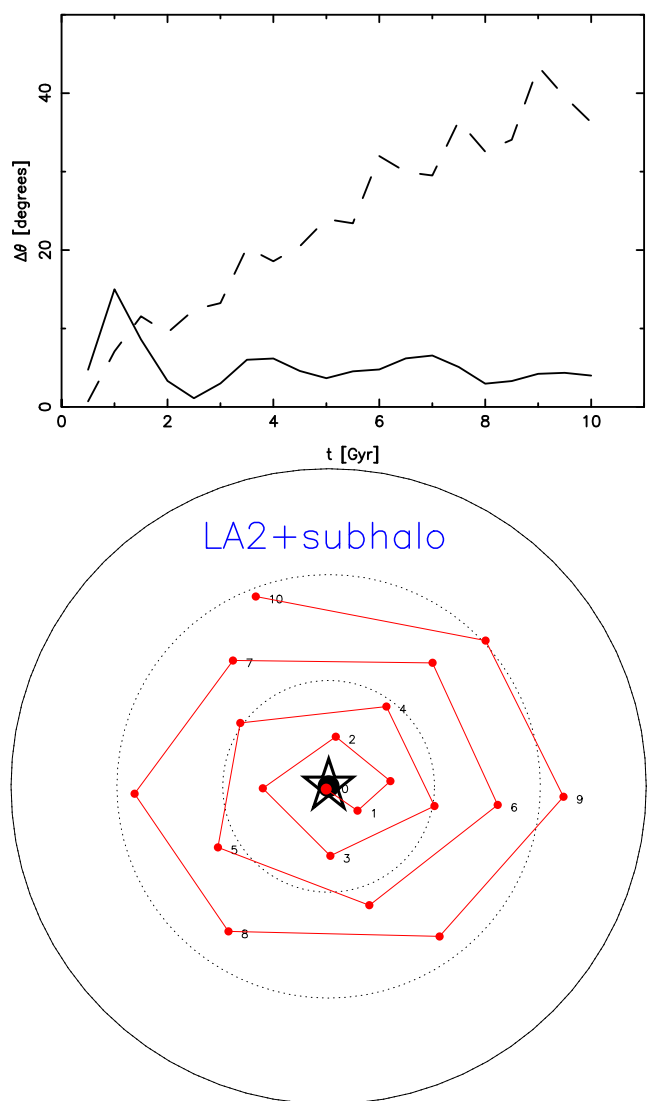

Figure 14. Top: disc tilting in models SA1 (solid line) and LA2 (dashed line) after the disc is perturbed by a substructure. Plotted is the angle between the instantaneous angular momentum vector and the initial one. Bottom: Briggs figure for model LA2 showing the evolution after it is perturbed by the substructure. Dotted circles are spaced by $20°$ with the outer solid circle corresponding to $\theta = 60°$. The disc spin is indicated by the filled (red and black) circles. The halo long axis is indicated by the black open star.

an internal, orbital perspective, our simulations capture the same physics as more complicated fully cosmological simulations.

There are, however, effects which our simulations do not capture. In the Λ cold dark matter (ΛCDM) universe, dark matter haloes (1) host a spectrum of substructure accounting for roughly 3–5 per cent of the total mass of the main halo itself at the present time (Diemand, Kuhlen & Madau 2007; Springel et al. 2008), (2) slowly tumble (Dubinski 1992; Bailin & Steinmetz 2004; Bryan & Cress 2007) (3) and gain mass. We now consider whether each of these differences alter our conclusions.

5.1.1 Halo substructure

We have shown here that satellites lead to red discs evolving to a short-axis orientation, which is the lowest energy state of the system. The role of the satellites is to provide the initial finite
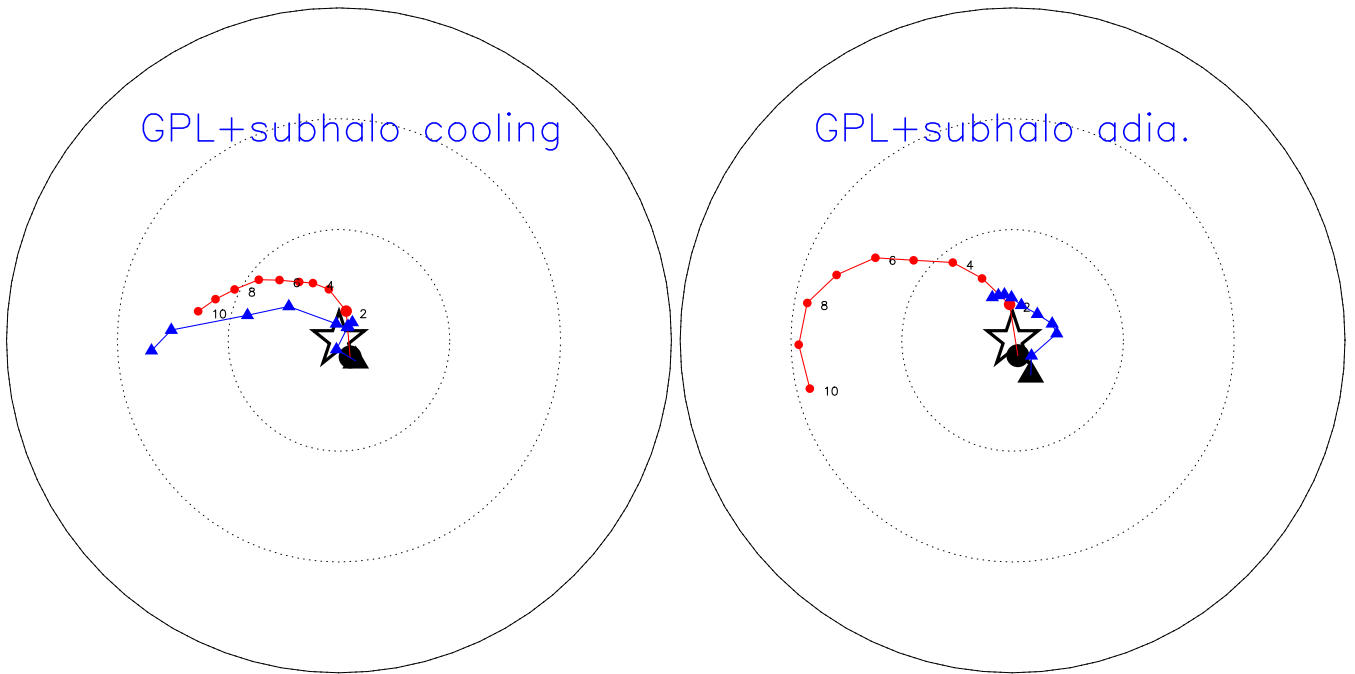
Figure 15. Briggs figures showing the evolution of model GPL perturbed by a subhalo with gas cooling and star formation (left) and evolved adiabatically (right). Dotted circles are spaced by $20°$. The disc spin is indicated by the filled (red and black) circles. The (blue and black) filled triangles mark the orientation of the hot gas angular momentum between 20 and 50 kpc. The spin of both the disc and gas at 1 Gyr are marked by the larger (black) corresponding symbols. The long axis of the halo is indicated by the (black) open star. The outer solid circle corresponds to $\theta = 60°$.

perturbation that allows halo torques to drive the disc to the short-axis orientation. For instance, a 2 per cent mass subhalo initially drives the disc of model LA2 from the long-axis orientation by $10°$, after which the torque from the triaxial halo takes over and drives the disc further away from the long-axis orientation. Therefore, the presence of a ΛCDM spectrum of subhaloes speeds up the rate at which initial perturbations build up but subsequently the evolution is dominated by the main halo itself. Kazantzidis et al. (2009) show that on average 5 subhaloes with mass > 20 per cent M_d pass within 20 kpc of the Galactic Centre since redshift $z = 1$. The cumulative effect of these ~$10°$ kicks is to ensure that the disc is never stuck in the local minimum provided by the long-axis orientation, instead ensuring that the disc is close to a short-axis orientation.

5.1.2 Halo figure rotation

Pattern rotation leads to warped planes of stable loop orbits. The measured pattern speeds of haloes in dark matter only simulations follows a log-normal distribution centred on $\Omega_p = 0.148\,h\,\mathrm{km\,s^{-1}\,kpc^{-1}}$. At these low tumbling rates, the region where stable loop orbits are warped is at relatively large radius (Binney 1978; Heisler, Merritt & Schwarzschild 1982; Magnenat 1982; Durisen et al. 1983; Lake & Norman 1983; Steiman-Cameron & Durisen 1984; Martinet & de Zeeuw 1988; Habe & Ikeuchi 1985, 1988; Deibel, Valluri & Merritt 2011). Deibel et al. (2011) find that as the pattern speed gets large, both box orbits and long-axis tube orbits are destabilized. Prograde short-axis tubes are also destabilized, but are replaced by retrograde short-axis tubes. These orbital changes can in principle alter the shapes of the haloes; however, even the slowest of Deibel et al. (2011)'s pattern speeds is about as large as the fastest pattern speeds of haloes found in dark matter-only simulations. Thus, in real haloes loop orbits at small radii should still be stable circulating about the short and long axes. The

short-axis orientation should therefore still be a stable orientation for stellar discs. We therefore conclude that the tumbling of dark matter haloes is not large enough to alter our conclusions.

5.1.3 Halo growth

Haloes are generally believed to be continuously growing. For instance the virial radius and concentration of haloes increase even at late times. However much of this is pseudo-evolution due to the changing critical density of the Universe, relative to which the virial radius and concentration parameters are defined. Diemer, More & Kravtsov (2013) show that for galaxy-sized haloes, $M_{200} \sim 10^{12}\,\mathrm{M_\odot}$ at $z = 0$, most of the evolution since $z = 1$ can be attributed to pseudo-evolution of this kind. Likewise, Prada et al. (2006) find little evolution in the outer regions of haloes in the mass range 10^{11}–$5 \times 10^{12}\,\mathrm{M_\odot}$. Thus, most disc galaxies will not experience significant halo growth. More massive haloes, which typically host elliptical galaxies, will still be growing rapidly and these will drive evolution not considered here.

5.1.4 Halo axes-ratios

One important difference between our simulations and cosmological ones is in the shapes of the haloes. The haloes in our simulations are generally quite elongated, with $0.32 \lesssim c/a \lesssim 0.55$; less than 3 per cent of haloes of mass $\log M_{200} \simeq 12.5$ in cosmological simulations have $c/a < 0.32$, while >16 per cent of haloes have $c/a < 0.55$ (Macciò et al. 2007; Macciò, Dutton & van den Bosch 2008; Schneider, Frenk & Cole 2012). Therefore, the torques from the dark matter haloes that the discs in the simulations experience are larger than what might be expected in general. This has the effect that it allows gasless discs to settle into a minor-axis orientation faster here than in nature. On the other hand, gas

cooling is able to tilt disc galaxies even more readily than in our simulations.

We conclude that while our simulations are idealized, they capture most of the physics relevant for the relative orientation of discs and haloes. The elongated shapes of our haloes may bias the galaxies into stronger alignment with their haloes, but we already find that gas dominates the disc alignment in the case that gas cools on to the disc, which makes the gas even more dominant when the haloes are rounder than here. DeBuhr, Ma & White (2012) presented cosmological simulations in which stellar discs were placed with their spin along either the short or the long axes of their haloes. They found that discs tumble significantly, particularly when they start out in the long-axis orientation, but generally remain aligned with one of the main axes inside 50 kpc. These results with a cosmological population of subhaloes and realistic halo tumbling rates are consistent with our findings, confirming that satellites destabilize discs in a long-axis orientation but do not alter the orientation of discs in the short-axis orientation quite so much.

5.2 Red galaxies

In the absence of gas cooling, the main driver of a disc's orientation relative to its triaxial halo is the stability of different orientations. Loop orbits are stable around the short and long axes, but not around the intermediate axis (Heiligman & Schwarzschild 1979; Schwarzschild 1979; Goodman & Schwarzschild 1981; Wilkinson & James 1982; Adams et al. 2007; Carpintero & Muzzio 2012). This has led to the expectation that discs spin around either the long or the short axis of a triaxial halo.

In the absence of gas, the orientation in which the disc's spin and halo's short axis align is always stable. Indeed this orientation has the lowest potential energy. We show that a disc can never remain with its spin aligned with the intermediate axis of the halo, even if the disc flattens the inner halo so much that the vertical direction is the halo's shortest axis throughout the disc. The equilibrium of discs orthogonal to the long axis of the halo is unstable, but the tilting rate is so low for massive discs that the orientation persists for a Hubble time and can be considered quasi-stable. However, perturbations from quite low-mass and low-concentration satellites will drive even massive discs away from this orientation, whereas a disc with its spin along the halo's short axis returns to that orientation soon after a satellite perturbs it.

Red galaxies will therefore tend to line up with their spin parallel to the short axis of the halo. Indeed studies using Sloan Digital Sky Survey (SDSS) have found that red galaxies have a satellite distribution which is aligned with their projected major axis (Sales & Lambas 2004; Brainerd 2005; Agustsson & Brainerd 2006; Yang et al. 2006; Bailin et al. 2008). Alignment is not however perfect, because discs do not settle into a short-axis orientation immediately.

We find that, at fixed mass, a disc in the long-axis orientation tilts much more rapidly when it has a larger scalelength. This occurs because more of the disc is exposed to the part of the potential that is perpendicular to the disc. A testable prediction of our simulations therefore is that, at fixed mass, red galaxies with larger half-mass radius should be more tightly coupled to their haloes and therefore show a stronger alignment.

5.3 Blue galaxies

The continued star formation activity of blue galaxies requires the accretion of gas (e.g. Sancisi et al. 2008). Cosmological simulations find that gas and dark matter angular momentum decoupling is common (e.g. Bailin et al. 2005; Croft et al. 2009; Bett et al. 2010; Hahn et al. 2010; Roškar et al. 2010). Our simulations show that, in order for the stellar disc to reach a balance between the gravitational torques and the angular momentum it gains from the halo the gas spin must in general be misaligned with the disc's, regardless of whether the gas is shock heated, or arrives via cold flows (Birnboim & Dekel 2003; Kereš et al. 2005; Dekel et al. 2009). This leads to star-forming blue discs remaining in almost arbitrary orientation. Rather than being perpendicular to the gas angular momentum, the disc tends to align itself at an orientation where the torque from the halo and the gas inflow balance. The supply of gas is therefore a much stronger driver of disc orientation than are gravitational torques from the halo, even when the halo globally has a quite prolate-triaxial shape. When the gas corona angular momentum orientation is evolving, the disc orientation also changes to remain in equilibrium between the halo torque and the inflowing gas angular momentum.

Fraternali & Tomassetti (2012) estimate a star formation rate of $\sim 3\,\mathrm{M_\odot}\,\mathrm{yr^{-1}}$ in the Milky Way. Assuming a Milky Way disc mass of $4\text{--}5 \times 10^{10}\,\mathrm{M_\odot}$, this corresponds to specific star formation rate (SSFR) $\dot{M}_*/M_* \sim 0.06\text{-}0.08\,\mathrm{Gyr^{-1}}$. While GP45 has a high star formation rate, $\sim 7\,\mathrm{M_\odot}\,\mathrm{yr^{-1}}$, the corresponding SSFR is $\dot{M}_*/M_* \sim 0.08\,\mathrm{Gyr^{-1}}$, in good agreement with the Milky Way. Thus, the SSFR, and presumably the cooling rates, in the simulations are characteristic of real galaxies and we can expect that galaxies like the Milky Way will be off the main planes of their dark matter haloes. At lower gas cooling rates, and lower SSFRs, gas cooling is no longer able to deliver sufficient angular momentum to the disc and the disc drops into a short-axis alignment with the halo.

Even in the presence of cooling gas the intermediate-axis orientation continues to be avoided. Since the distribution of orientations avoids one axis, this introduces a weak correlation between the halo long axis and disc spin. D13 found that the stellar disc that forms when gas angular momentum is along the intermediate axis is never closer to it than $20°$. Detailed modelling, which will be presented elsewhere, suggests that this tendency to avoid alignment along the intermediate axis results in a weak *anti-correlation* between the major axis of the disc and the projected major axis of its host halo. The observed, weak alignments for blue galaxies therefore either require a correlation between the gas angular momentum and the large scale structure, or a contribution from galaxies in which the gas inflow rate is insufficient to (significantly) impact the orientation of the disc.

The observed difference in relative orientation of disc and halo between red and blue galaxies is additional evidence that star-forming galaxies need to continuously accrete gas to maintain their star formation. Without the inflow of misaligned angular momentum, torques from triaxial haloes and perturbations from subhaloes would drive the discs of blue galaxies to an alignment similar to that of red galaxies. The important difference between blue and red galaxies is not the presence of gas and star formation but the cosmic infall of gas with misaligned angular momentum with some of this gas cooling on to the stellar disc. A galaxy slowly forming stars from only a pre-existing gas disc/inner corona (including the recycling of gas via feedback and a fountain) will still tend to evolve towards a short-axis orientation.

5.4 The Milky Way and Andromeda

The shape of the Milky Way's dark matter halo has been modelled numerous times via the Sagittarius stream. To date the best-fitting

models have needed a triaxial halo, but have required that the disc is perpendicular to the intermediate axis of the halo (Law et al. 2009; Law & Majewski 2010; Deg & Widrow 2013; Vera-Ciro & Helmi 2013). D13 showed that this orientation is particularly unstable and very unlikely even if the inner halo is flattened. By a process of elimination, they concluded that the Milky Way must be tilted with respect to the principal planes of the halo. Deg & Widrow (2014), using mock data of a disc tilted relative to the halo, showed that modelling under the incorrect assumption that the disc lies in one of the main planes of the halo leads to a best-fitting model with the disc perpendicular to the intermediate axis of the halo. This may explain the persistent finding that the Milky Way is perpendicular to its halo's intermediate axis.

The case for a tilted disc in Andromeda is suggested by the distribution of a fraction of the satellites around it, which Ibata et al. (2013) showed consists of a thin disc inclined relative to the main plane of the stellar disc. Bowden, Evans & Belokurov (2013) show that the satellite disc must lie perpendicular to the long or the short axis of the halo if the satellite disc is long lived and the halo is not spherical, suggesting that the main stellar disc is inclined relative to the halo.

5.5 Summary

Our main results can be summarized as follows.

(i) A stellar disc without gas can persist indefinitely with its spin along the short axis of a triaxial halo. Even when perturbed by a satellite, the disc quickly settles back to this orientation. Instead if a stellar disc starts with its spin aligned with the long axis of the halo, whether the disc remains in this orientation or not depends on the shape of the halo potential. At low stellar mass, the potential surrounding the disc is orthogonal to it and the disc tilts towards a short-axis orientation. On the other hand, when the disc is massive it flattens the total potential and it usually can persist in this orientation for a long time. Perturbations by satellites however permanently drive a disc off the long-axis orientation. Finally, not even a very massive stellar disc is stable perpendicular to the intermediate axis of the dark matter halo, even when the inner halo becomes flattened. Thus, the most natural orientation for gasless red discs is with their spins along the short axis of the halo.

(ii) A disc with gas cooling on to it settles into equilibrium between the angular momentum it gains from the gas and the torques it feels from the halo and gas corona. The disc is therefore not perpendicular to the axes of the halo (unless the gas spin is about the short or the long axis) nor is it perpendicular to the spin of the gas. If the orientation of the gas angular momentum evolves, then the orientation of the disc is also forced to change.

(iii) These simulations therefore imply that while gas poor, red galaxies tend to align with their spins along the short axis of their haloes, the infall of gas on to blue galaxies allows them to linger at a wide range of orientations relative to the halo. Thus, stacking blue haloes lead to a nearly isotropic distribution. The need to avoid the intermediate-axis orientation introduces a weak anticorrelation between the disc and the halo major axis.

(iv) Our simulations show that the relative orientations of discs and haloes are set by local conditions, i.e. those within the virial radius of the halo.

ACKNOWLEDGEMENTS

REFERENCES

Adams F. C., Bloch A. M., Butler S. C., Druce J. M., Ketchum J. A., 2007, ApJ, 670, 1027
Agustsson I., Brainerd T. G., 2006, ApJ, 644, L25
Allgood B., Flores R. A., Primack J. R., Kravtsov A. V., Wechsler R. H., Faltenbacher A., Bullock J. S., 2006, MNRAS, 367, 1781
Aragón-Calvo M. A., van de Weygaert R., Jones B. J. T., van der Hulst J. M., 2007, ApJ, 655, L5
Aumer M., White S. D. M., 2013, MNRAS, 428, 1055
Azzaro M., Patiri S. G., Prada F., Zentner A. R., 2007, MNRAS, 376, L43
Bailin J., Steinmetz M., 2004, ApJ, 616, 27
Bailin J., Steinmetz M., 2005, ApJ, 627, 647
Bailin J. et al., 2005, ApJ, 627, L17
Bailin J., Power C., Norberg P., Zaritsky D., Gibson B. K., 2008, MNRAS, 390, 1133
Bardeen J. M., Bond J. R., Kaiser N., Szalay A. S., 1986, ApJ, 304, 15
Barnes J., Efstathiou G., 1987, ApJ, 319, 575
Bett P., Eke V., Frenk C. S., Jenkins A., Okamoto T., 2010, MNRAS, 404, 1137
Binggeli B., 1982, A&A, 107, 338
Binney J., 1978, MNRAS, 183, 779
Birnboim Y., Dekel A., 2003, MNRAS, 345, 349
Bowden A., Evans N. W., Belokurov V., 2013, MNRAS, 435, 928
Brainerd T. G., 2005, ApJ, 628, L101
Bridle S., King L., 2007, New J. Phys., 9, 444
Briggs F. H., 1990, ApJ, 352, 15
Brown M. L., Taylor A. N., Hambly N. C., Dye S., 2002, MNRAS, 333, 501
Bryan S. E., Cress C. M., 2007, MNRAS, 380, 657
Bullock J. S., Dekel A., Kolatt T. S., Kravtsov A. V., Klypin A. A., Porciani C., Primack J. R., 2001, ApJ, 555, 240
Camelio G., Lombardi M., 2015, A&A, 575, A113
Carpintero D. D., Muzzio J. C., 2012, Celest. Mech. Dyn. Astron., 112, 107
Carter D., Metcalfe N., 1980, MNRAS, 191, 325
Catelan P., Porciani C., 2001, MNRAS, 323, 713
Catelan P., Kamionkowski M., Blandford R. D., 2001, MNRAS, 320, L7
Chen D. N., Jing Y. P., Yoshikaw K., 2003, ApJ, 597, 35
Ciotti L., Dutta S. N., 1994, MNRAS, 270, 390
Codis S., Pichon C., Devriendt J., Slyz A., Pogosyan D., Dubois Y., Sousbie T., 2012, MNRAS, 427, 3320
Crittenden R. G., Natarajan P., Pen U.-L., Theuns T., 2001, ApJ, 559, 552
Croft R. A. C., Metzler C. A., 2000, ApJ, 545, 561

Croft R. A. C., Di Matteo T., Springel V., Hernquist L., 2009, MNRAS, 400, 43

Cuesta A. J., Betancort-Rijo J. E., Gottlöber S., Patiri S. G., Yepes G., Prada F., 2008, MNRAS, 385, 867

Debattista V. P., Sellwood J. A., 2000, ApJ, 543, 704

Debattista V. P., Moore B., Quinn T., Kazantzidis S., Maas R., Mayer L., Read J., Stadel J., 2008, ApJ, 681, 1076 (D08)

Debattista V. P., Roškar R., Valluri M., Quinn T., Moore B., Wadsley J., 2013, MNRAS, 434, 2971 (D13)

DeBuhr J., Ma C.-P., White S. D. M., 2012, MNRAS, 426, 983

Deg N., Widrow L., 2013, MNRAS, 428, 912

Deg N., Widrow L., 2014, MNRAS, 439, 2678

Deibel A. T., Valluri M., Merritt D., 2011, ApJ, 728, 128

Dekel A. et al., 2009, Nature, 457, 451

Diemand J., Kuhlen M., Madau P., 2007, ApJ, 657, 262

Diemer B., More S., Kravtsov A. V., 2013, ApJ, 766, 25

Dubinski J., 1992, ApJ, 401, 441

Dubinski J., Carlberg R. G., 1991, ApJ, 378, 496

Durisen R. H., Tohline J. E., Burns J. A., Dobrovolskis A. R., 1983, ApJ, 264, 392

Emsellem E. et al., 2011, MNRAS, 414, 888

Faltenbacher A., Allgood B., Gottlöber S., Yepes G., Hoffman Y., 2005, MNRAS, 362, 1099

Faltenbacher A., Li C., Mao S., van den Bosch F. C., Yang X., Jing Y. P., Pasquali A., Mo H. J., 2007, ApJ, 662, L71

Faltenbacher A., Jing Y. P., Li C., Mao S., Mo H. J., Pasquali A., van den Bosch F. C., 2008, ApJ, 675, 146

Faltenbacher A., Li C., White S. D. M., Jing Y.-P., Shu-DeMao, Wang J., 2009, Res. Astron. Astrophys., 9, 41

Fleck J.-J., Kuhn J. R., 2003, ApJ, 592, 147

Franx M., Illingworth G., de Zeeuw T., 1991, ApJ, 383, 112

Fraternali F., Tomassetti M., 2012, MNRAS, 426, 2166

Frenk C. S., White S. D. M., Davis M., Efstathiou G., 1988, ApJ, 327, 507

Goodman J., Schwarzschild M., 1981, ApJ, 245, 1087

Green J. et al., 2011, preprint (arXiv:e-prints)

Habe A., Ikeuchi S., 1985, ApJ, 289, 540

Habe A., Ikeuchi S., 1988, ApJ, 326, 84

Hahn O., Porciani C., Carollo C. M., Dekel A., 2007a, MNRAS, 375, 489

Hahn O., Carollo C. M., Porciani C., Dekel A., 2007b, MNRAS, 381, 41

Hahn O., Teyssier R., Carollo C. M., 2010, MNRAS, 405, 274

Hao J., Kubo J. M., Feldmann R., Annis J., Johnston D. E., Lin H., McKay T. A., 2011, ApJ, 740, 39

Heavens A., Refregier A., Heymans C., 2000, MNRAS, 319, 649

Heiligman G., Schwarzschild M., 1979, ApJ, 233, 872

Heisler J., Merritt D., Schwarzschild M., 1982, ApJ, 258, 490

Heymans C., Brown M., Heavens A., Meisenheimer K., Taylor A., Wolf C., 2004, MNRAS, 347, 895

Hirata C. M., Mandelbaum R., Ishak M., Seljak U., Nichol R., Pimbblet K. A., Ross N. P., Wake D., 2007, MNRAS, 381, 1197

Huang S., Carlberg R. G., 1997, ApJ, 480, 503

Ibata R. A. et al., 2013, Nature, 493, 62

Ivezic Z. et al., 2008, preprint (arXiv:e-prints)

Jing Y. P., 2002, MNRAS, 335, L89

Jing Y. P., Suto Y., 2002, ApJ, 574, 538

Joachimi B., Semboloni E., Bett P. E., Hartlap J., Hilbert S., Hoekstra H., Schneider P., Schrabback T., 2013a, MNRAS, 431, 477

Joachimi B., Semboloni E., Hilbert S., Bett P. E., Hartlap J., Hoekstra H., Schneider P., 2013b, MNRAS, 436, 819

Kang X., van den Bosch F. C., Yang X., Mao S., Mo H. J., Li C., Jing Y. P., 2007, MNRAS, 378, 1531

Kazantzidis S., Kravtsov A. V., Zentner A. R., Allgood B., Nagai D., Moore B., 2004, ApJ, 611, L73

Kazantzidis S., Magorrian J., Moore B., 2004, ApJ, 601, 37

Kazantzidis S., Zentner A. R., Kravtsov A. V., Bullock J. S., Debattista V. P., 2009, ApJ, 700, 1896

Kereš D., Katz N., Weinberg D. H., Davé R., 2005, MNRAS, 363, 2

Kirk D., Rassat A., Host O., Bridle S., 2012, MNRAS, 424, 1647

Kuhlen M., Diemand J., Madau P., 2007, ApJ, 671, 1135

Lake G., Norman C., 1983, ApJ, 270, 51

Laureijs R. et al., 2011, preprint (arXiv:e-prints)

Law D. R., Majewski S. R., 2010, ApJ, 714, 229

Law D. R., Majewski S. R., Johnston K. V., 2009, ApJ, 703, L67

Lee J., Pen U.-L., 2007, ApJ, 670, L1

Li Z., Wang Y., Yang X., Chen X., Xie L., Wang X., 2013, ApJ, 768, 20

Libeskind N. I., Hoffman Y., Knebe A., Steinmetz M., Gottlöber S., Metuki O., Yepes G., 2012, MNRAS, 421, L137

Macciò A. V., Dutton A. A., van den Bosch F. C., Moore B., Potter D., Stadel J., 2007, MNRAS, 378, 55

Macciò A. V., Dutton A. A., van den Bosch F. C., 2008, MNRAS, 391, 1940

Magnenat P., 1982, A&A, 108, 89

Mandelbaum R., Hirata C. M., Ishak M., Seljak U., Brinkmann J., 2006, MNRAS, 367, 611

Martinet L., de Zeeuw T., 1988, A&A, 206, 269

Miller G. E., Scalo J. M., 1979, ApJS, 41, 513

Moore B., Kazantzidis S., Diemand J., Stadel J., 2004, MNRAS, 354, 522

Nierenberg A. M., Auger M. W., Treu T., Marshall P. J., Fassnacht C. D., 2011, ApJ, 731, 44

Okumura T., Jing Y. P., Li C., 2009, ApJ, 694, 214

Paz D. J., Stasyszyn F., Padilla N. D., 2008, MNRAS, 389, 1127

Pen U.-L., Lee J., Seljak U., 2000, ApJ, 543, L107

Pereira M. J., Kuhn J. R., 2005, ApJ, 627, L21

Pereira M. J., Bryan G. L., Gill S. P. D., 2008, ApJ, 672, 825

Plionis M., 1994, ApJS, 95, 401

Porciani C., Dekel A., Hoffman Y., 2002, MNRAS, 332, 325

Prada F., Klypin A. A., Simonneau E., Betancort-Rijo J., Patiri S., Gottlöber S., Sanchez-Conde M. A., 2006, ApJ, 645, 1001

Roškar R., Debattista V. P., Stinson G. S., Quinn T. R., Kaufmann T., Wadsley J., 2008, ApJ, 675, L65

Roškar R., Debattista V. P., Brooks A. M., Quinn T. R., Brook C. B., Governato F., Dalcanton J. J., Wadsley J., 2010, MNRAS, 408, 783

Roškar R., Debattista V. P., Quinn T. R., Wadsley J., 2012, MNRAS, 426, 2089

Roškar R., Debattista V. P., Loebman S. R., 2013, MNRAS, 433, 976

Sales L., Lambas D. G., 2004, MNRAS, 348, 1236

Sancisi R., Fraternali F., Oosterloo T., van der Hulst T., 2008, A&AR, 15, 189

Schneider M. D., Frenk C. S., Cole S., 2012, J. Cosmol. Astropart. Phys., 5, 30

Schneider M. D. et al., 2013, MNRAS, 433, 2727

Schwarzschild M., 1979, ApJ, 232, 236

Sellwood J. A., 2003, ApJ, 587, 638

Sharma S., Steinmetz M., 2005, ApJ, 628, 21

Smargon A., Mandelbaum R., Bahcall N., Niederste-Ostholt M., 2012, MNRAS, 423, 856

Soares-Santos M., DES Collaboration, 2012, J. Phys. Conf. Ser., 375, 032006

Springel V. et al., 2008, MNRAS, 391, 1685

Stadel J. G., 2001, PhD thesis, Univ. Washington

Steiman-Cameron T. Y., Durisen R. H., 1984, ApJ, 276, 101

Stinson G., Seth A., Katz N., Wadsley J., Governato F., Quinn T., 2006, MNRAS, 373, 1074

Struble M. F., 1990, AJ, 99, 743

Tempel E., Libeskind N. I., 2013, ApJ, 775, L42

Tempel E., Stoica R. S., Saar E., 2013, MNRAS, 428, 1827

Trowland H. E., Lewis G. F., Bland-Hawthorn J., 2013, ApJ, 762, 72

Troxel M. A., Ishak M., 2015, Phys. Rep., 558, 1

Usami M., Fujimoto M., 1997, ApJ, 487, 489

Valluri M., Debattista V. P., Quinn T., Moore B., 2010, MNRAS, 403, 525

Valluri M., Debattista V. P., Quinn T. R., Roškar R., Wadsley J., 2012, MNRAS, 419, 1951

Valluri M., Debattista V. P., Stinson G. S., Bailin J., Quinn T. R., Couchman H. M. P., Wadsley J., 2013, ApJ, 767, 93

van den Bosch F. C., Abel T., Croft R. A. C., Hernquist L., White S. D. M., 2002, ApJ, 576, 21

van Haarlem M., van de Weygaert R., 1993, ApJ, 418, 544

Vera-Ciro C., Helmi A., 2013, ApJ, 773, L4

Wadsley J. W., Stadel J., Quinn T., 2004, New Astron., 9, 137

Wang Y., Yang X., Mo H. J., Li C., van den Bosch F. C., Fan Z., Chen X., 2008a, MNRAS, 385, 1511

Wang Y., Yang X., Mo H. J., van den Bosch F. C., Weinmann S. M., Chu Y., 2008b, ApJ, 687, 919

Wang Y., Park C., Hwang H. S., Chen X., 2010, ApJ, 718, 762

Wang H., Mo H. J., Jing Y. P., Yang X., Wang Y., 2011, MNRAS, 413, 1973

Warren M. S., Quinn P. J., Salmon J. K., Zurek W. H., 1992, ApJ, 399, 405

Wilkinson A., James R. A., 1982, MNRAS, 199, 171

Yang X., van den Bosch F. C., Mo H. J., Mao S., Kang X., Weinmann S. M., Guo Y., Jing Y. P., 2006, MNRAS, 369, 1293

Zhang Y., Yang X., Faltenbacher A., Springel V., Lin W., Wang H., 2009, ApJ, 706, 747

Zhang Y., Yang X., Wang H., Wang L., Mo H. J., van den Bosch F. C., 2013, ApJ, 779, 160

Zhang Y., Yang X., Wang H., Wang L., Luo W., Mo H. J., van den Bosch F. C., 2015, ApJ, 798, 17

This paper has been typeset from a TEX/LATEX file prepared by the author.